Chem

Article

Transition-path times of individual molecular shuttles under mechanical equilibrium show symmetry

Graphical abstract

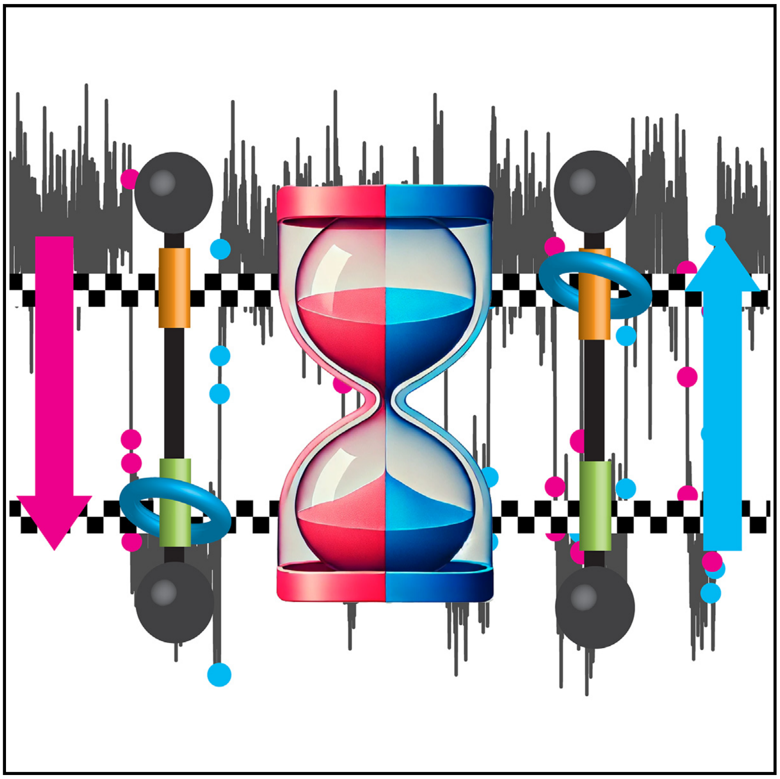

Authors

Tomás Nicolás-García,
Natalia Martín Sabanés,
Rebeca Bocanegra, R. Dean Astumian,
Emilio M. Pérez, Borja Ibarra

Correspondence

emilio.perez@imdea.org (E.M.P.),
borja.ibarra@imdea.org (B.I.)

In brief

This study explores microscopic reversibility to understand the operation of molecular devices.

Highlights

- Identification of transition paths on individual molecular shuttles
- Transition paths were statistically independent and highly variable
- Transition paths were symmetrically distributed, proving microscopic reversibility
- Analysis of transition paths provided thermodynamic insights into shuttling motion

9 INDUSTRY, INNOVATION AND INFRASTRUCTURE

Nicolás-García et al., 2025, Chem *11*, 102410
June 12, 2025
https://doi.org/10.1016/j.chempr.2024.102410

CellPress

Please cite this article in press as: Nicolás-García et al., Transition-path times of individual molecular shuttles under mechanical equilibrium show symmetry, Chem (2025), https://doi.org/10.1016/j.chempr.2024.102410

Chem

CellPress
OPEN ACCESS

Article

Transition-path times of individual molecular shuttles under mechanical equilibrium show symmetry

Tomás Nicolás-García,[1,3] Natalia Martín Sabanés,[1,3] Rebeca Bocanegra,[1] R. Dean Astumian,[2] Emilio M. Pérez,[1,*] and Borja Ibarra[1,4,*]
[1]IMDEA Nanociencia, Faraday 9, Campus de Cantoblanco, 28049 Madrid, Spain
[2]Department of Physics and Astronomy, University of Maine, Orono, ME 04469, USA
[3]These authors contributed equally
[4]Lead contact
*Correspondence: emilio.perez@imdea.org (E.M.P.), borja.ibarra@imdea.org (B.I.)
https://doi.org/10.1016/j.chempr.2024.102410

THE BIGGER PICTURE Molecular shuttles are bistable devices in which a macrocycle threaded onto a linear component transitions between two different positions in response to external stimuli. We used optical tweezers to identify the transition paths of shuttling events recorded on individual molecular shuttles under mechanical equilibrium. We confirmed experimentally that the transition paths show symmetry. The properties of these transition paths contain fundamental mechanistic information about the shuttling process. Our study paves the way to explore the temporal sequence of events during shuttling and investigate the possibility of taking multiple paths through the energy landscape. Additionally, we will be able to determine the effect of external stimuli and the chemical composition of the molecular shuttle on the properties of transition paths under nonequilibrium conditions. This information is pivotal in the design and optimization of molecular shuttles for diverse nanotechnological applications.

SUMMARY

Measuring individual trajectories during the operation of synthetic devices is crucial for a thorough understanding of this operation. Here, we use optical tweezers to measure individual transition paths of molecular shuttles under mechanical equilibrium. Our results showed that the transition-path times present wide distributions, indicating a statistically independent and variable behavior while maintaining a time-reversal symmetry derived from the principle of microscopic reversibility. Furthermore, we show that thermodynamic variables can be extracted from the transition-path times using the principle of microscopic reversibility. These measurements provide a first experimental look at the principle of microscopic reversibility in molecular shuttles and pave the way for a detailed and quantitative understanding of the dynamics of synthetic molecular machines.

INTRODUCTION

Biological systems and synthetic molecular devices both rely on thermal energy to move their constituent parts to carry out their functions.[1] These long-range motions occur along pathways connecting each sequential step from the initial to the final state.[2] The details of these transition paths contain fundamental information about the transition states and the mechanism(s) that drive(s) the overall process, i.e., protein/nucleic acid folding[3–7] or the shuttling of a macrocycle in synthetic molecular shuttles. Molecular shuttles are bistable devices that transition between two different equilibrating co-conformations in response to external stimuli.[8,9] In molecular shuttles, a macrocycle trapped onto a linear component (axle) can be reversibly moved between two chemically different regions of the thread (stations) separated along the axle. These stations bind to the macrocycle noncovalently with different affinities. Modification of the relative affinities of the stations for the macrocycle by external stimuli (i.e., pH,[10] light,[11,12] chemical stimulation,[13,14] or mechanical force[15]) changes the time it spends at each station while it hops back and forth by random thermal motion. The bistability and controlled shuttling motion characteristic of these devices make them suitable as fundamental components in diverse nanotechnological applications.[16–19] Therefore, understanding the microscopic mechanisms of the shuttling process would be pivotal in the design and

Please cite this article in press as: Nicolás-García et al., Transition-path times of individual molecular shuttles under mechanical equilibrium show symmetry, Chem (2025), https://doi.org/10.1016/j.chempr.2024.102410

optimization of the performance of these devices at the molecular level. Shuttling involves (1) passage through a high-energy transition state forming an energy barrier between stable states and (2) the paths (that pass or transition) through these states. The properties of these transition paths (i.e., duration, velocity, and shape) contain all the fundamental mechanistic information about the shuttling process.

Molecular shuttles are expected to present well-defined transition paths between their two main co-conformations. These transition paths have been studied theoretically,[20,21] but their short lifetimes, much shorter than the lifetime of residence of the macrocycle at the stations, as well as their intrinsic stochastic nature, have prevented their direct observation experimentally. This limits our understanding of the working mechanisms that govern the dynamics in the energy landscapes of these molecular devices. Despite significant research efforts to shed light on this issue, only indirect strategies for characterizing average transition states have been achieved. For example, Panman et al. studied the shuttling mechanism of a redox-activated molecular shuttle through time-resolved vibrational spectroscopy.[22] They monitored the changes in the frequencies of the carbonyl stretch, present in both stations, to determine when the macrocycle left one station and arrived at the other (or returned to the initial station). The rates of forward and backward shuttling can also be extracted from analysis of thermodynamic parameters determined by absorption spectroscopy,[23] nuclear magnetic resonance,[24] or electrochemistry.[25] However, direct experimental measurements of the transition pathways at the nanoscale are needed to fully understand the nature of shuttling in artificial molecular devices.

Single-molecule manipulation methods such as atomic force microscopy,[26] scanning tunneling microscopy,[27] or single-molecule junctions[28] have only recently started to be applied to the investigation of synthetic molecular devices.[29] These techniques have led to breakthroughs like the measurement of the work exerted against a load by molecular devices,[30,31] or more directly related to this work, the observation of an intermediate state in the shuttling between two stations in a H-bonded molecular shuttle.[32] Advances in optical tweezers have enabled the observation of transition paths in the folding of single biomolecules.[3,5,33,34] Recently, we reported the application of optical tweezers to extract the real-time kinetics of shuttling of individual molecular shuttles in aqueous solution.[35] Here, we used optical tweezers to unequivocally identify transition paths from hundreds of shuttling events recorded on individual molecular shuttles under mechanical equilibrium. Our measurements showed a wide distribution of transition-path times, indicating that each transition across the energy barrier was statistically independent and highly variable. We studied the shuttling process and found that transition-path times are symmetrically distributed. This was confirmed by comparing the last-touch first-touch times (LTFT) in both directions of shuttling Additionally, we used the experimental data to extract the energy profile of the shuttling process from transition-path probabilities.[36–39] Our theoretical analysis takes advantage of the fact that all molecules in solution are in mechanical equilibrium, regardless of whether the overall system is in thermodynamic equilibrium.

RESULTS AND DISCUSSION

Real-time monitoring of shuttling events

We synthetized a hydrogen-bonded Leigh-type molecular shuttle[40] featuring a benzylic amide macrocycle mechanically locked onto an oligoethylene glycol axel by two diphenylethyl stoppers (Figures 1A and S1–S16; supplemental information). The axel contains fumaramide (*fum*) and succinic amide-ester (*succ*) groups (or stations) separated by a 5.5 nm oligoethylene glycol spacer (retrieved from density functional theory [DFT] calculations, Figure S2), which is significantly shorter than that in our previous work[35] to facilitate synthesis. The stations interact through hydrogen bonds with the macrocycle with different affinities, producing a biased *fum*:*succ* occupancy ratio >95:5 (even in polar solvents).[41] In order to interface the molecule with the optical tweezers, the macrocycle was designed to contain an azide group and the stopper adjacent to the *fum* station was labeled with biotin. We used two double stranded (ds) DNA molecules, acting as handles, to individually manipulate single molecular shuttles (Figure 1B). One of the dsDNA handles is attached to the macrocycle via click chemistry, connecting it to a micron-size polystyrene bead held in the optical trap (our force and distance sensor). The other handle connects the biotin-labeled stopper to a bead fixed on top of a micropipette tip (see further information about the experimental setup in the supplemental information). Experiments were performed under aqueous conditions (20 mM Tris-HCl pH 7.5, 150 mM NaCl) at 22°C ± 1°C.

Initially, individual molecular shuttle-dsDNA hybrids were subjected to pulling-relaxing cycles to obtain histograms for the rupture forces at each station and calculate the coexistence force ($F_{1/2}$), or the force under which the macrocycle has an equal probability of residing over the *fum* or *succ* stations (Figure S17). This is done by retracting the optical trap relative to the micropipette tip at a constant pulling speed of 200 nm/s. Next, we kept a constant force on the molecular shuttle-dsDNA hybrid close to $F_{1/2}$ to maximize the number of shuttling transitions of the macrocycle between *fum* and *succ* stations (Figure 1C). We noted that the shuttling distance obtained experimentally (distance between the center of the *fum* and *succ* stations in Figure 1C) is affected by the length of the dsDNA handles. The expected distance (5.5 nm) can be recovered using shorter and stiffer dsDNA handles. The length of the handles does not affect the microscopic reversibility results relevant here (see below) in any of the experiments, and shuttling events presented well-defined residence or waiting times at each station and much faster transition times from one station to the other (Figures 1D, S18, and S19). Hence, we have continued to use the lengthy dsDNA handles in this study, as they facilitate detection and manipulation. Our experimental setup allowed recording hundreds of individual shuttling events for single molecular shuttle-dsDNA hybrids with millisecond temporal resolution yielding robust statistics for posterior analysis.

Microscopic reversibility of transition-path times measured on individual molecular shuttles

The transition-path time of the shuttling between stations (τ_{ts}) is defined as the time it takes for the macrocycle to travel from

Please cite this article in press as: Nicolás-García et al., Transition-path times of individual molecular shuttles under mechanical equilibrium show symmetry, Chem (2025), https://doi.org/10.1016/j.chempr.2024.102410

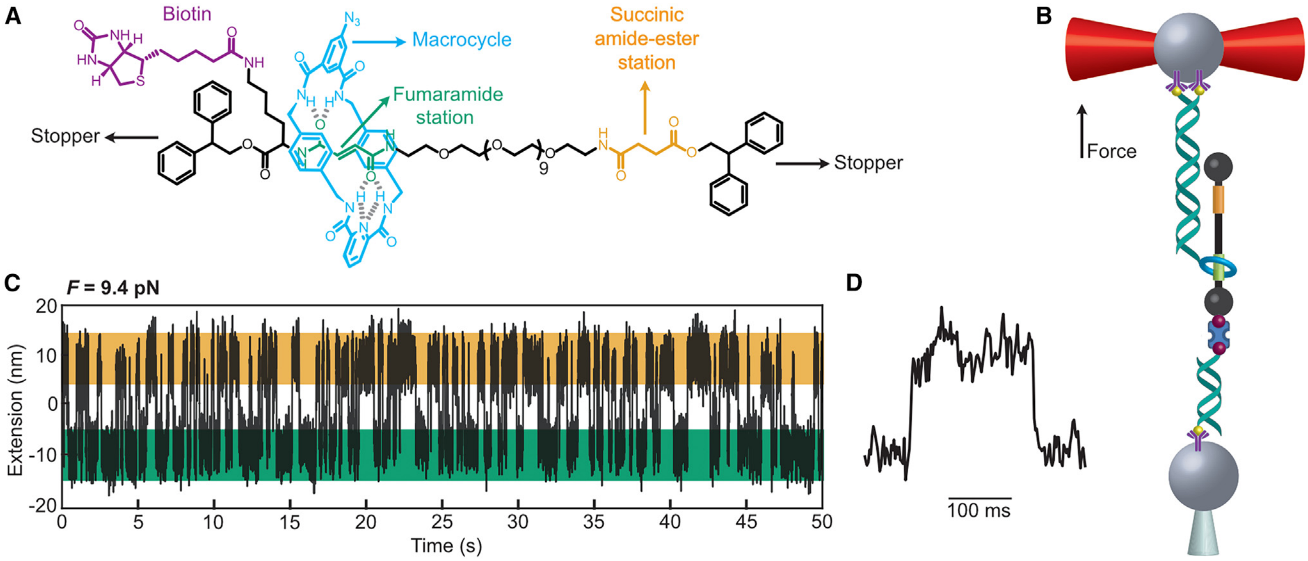

Figure 1. Chemical structure of the molecular shuttle, experimental setup, and measurement of individual shuttling events

(A) Chemical structure of the molecular shuttle. The macrocycle (in blue) is bound to the thermodynamically favored fumaramide station (*fum*, in green) by hydrogen bonding. External stimuli (here external mechanical force) shift the binding equilibrium of the macrocycle toward the succinic amide-ester station (*succ*, in orange).

(B) Diagram of the experimental setup (not to scale). The molecular shuttle is attached to two polystyrene beads (diameter ~3 μm) through two dsDNA handles. One handle connects the macrocycle to the bead in the optical trap (k = 0.13 pN nm^{-1}, laser power = 60 mW) via digoxigenin-anti-digoxigenin connections (yellow spheres). The other handle connects the terminal biotin of the thread (in purple) to a bead held by suction on top of a micropipette tip via biotin-streptavidin connections at one end and digoxigenin-anti-digoxigenin at the other. Load (force) is applied to the system by moving the optical trap relative to the micropipette tip.

(C) Representative hopping trace at constant force (9.4 pN) in which the sub-molecular motion of an individual macrocycle between *fum* (green stripe) and *succ* (orange stripe) stations is tracked in real time.

(D) Zoom-in on (C) in which two complete individual shuttling events take place. Scale bar: 100 ms.

one thermodynamic state to another. From mechanical equilibrium trajectories of the extension of the molecule (extension vs. time at a constant force), τ_{ts} was measured directly as the time required to cross between *a* and *b* limits (Figure 2, see also supplemental information for details on τ_{ts} calculation). These boundaries were chosen as half the mean position of *fum* and *succ*.[3] Data analysis showed that the mean values of τ_{ts} for *fum* → *succ* and *succ* → *fum* transitions are identical within error. The transition-path times presented broad distributions indicating that each transition across the barrier was statistically independent and highly variable. These distributions showed similar shapes for the forward and reverse reactions. The symmetry of the transition-path time distributions was confirmed independently by a two-sample Kolmogorov-Smirnov test and a Mann-Whitney U-test (Table S1) in accordance to the principle of microscopic reversibility.[34,42–45] The values of τ_{ts} obtained are in good agreement with transit times calculated indirectly taking into consideration the kinetic rates between stations, confirming the validity of our experimental data (Table S2; Figures S20 and S21).[3,42,46]

The time reversal shown for the specific case of the transit time should be held for any random points *a* and *b* within the macrocycle's trajectory either when equilibrium is shifted toward *fum* or *succ* stations, as predicted previously by Bier and Astumian. The LTFT time (the time elapsed between the moment the macrocycle last touches point *a* and first touches point *b*) must obey the LTFT relation[20,36,47]: $\tau_{LTFT}(a \rightarrow b) = \tau_{LTFT}(b \rightarrow a)$.

In Figure 3, we present the calculation of τ_{LTFT} in different hopping traces acquired at constant forces, where equilibrium shifts differently toward *fum* or *succ* stations. In this case, the boundaries *a* and *b* were chosen close to the mean position of *fum* and *succ* stations, respectively. The distribution of $\tau_{LTFT}(a \rightarrow b)$ was found to be symmetrical to that of $\tau_{LTFT}(b \rightarrow a)$ at all forces, confirming the LTFT principle. Symmetry was further corroborated by two-sample Kolmogorov-Smirnov and Mann-Whitney U tests (Table S3). Furthermore, we found that the symmetry of the LTFT distributions holds independently of the values chosen for boundaries *a* and *b* (Figures S22 and S23; Tables S4 and S5).

Calculation of energy landscapes from transition-path probabilities

Microscopic reversibility was applied by Bier and Astumian for cases when particles are subjected to an external driving bias, such as the mechanical force in our experiments.[47] Their corollary to microscopic reversibility takes advantage of the fact that the Onsager-Machlup relations require a linear relationship between force and velocity, which is characteristic of low Reynolds number behavior in single molecules.[48] As discussed by Bier et al.,[35] the relation for the ratio of the transition

Please cite this article in press as: Nicolás-García et al., Transition-path times of individual molecular shuttles under mechanical equilibrium show symmetry, Chem (2025), https://doi.org/10.1016/j.chempr.2024.102410

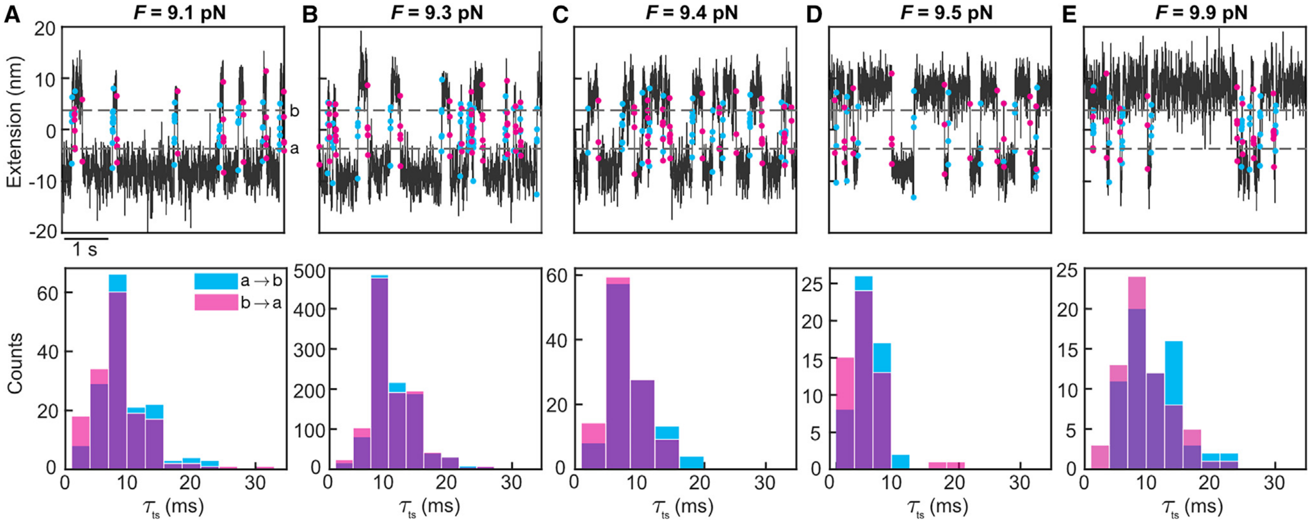

Figure 2. Distributions of transition-path times (τ_{ts}) of the shuttling between stations

Segment of hopping traces (top) acquired at constant forces below (A and B), close to (C), and above (D) coexistence, along with their corresponding transit time distributions (bottom) for *a* → *b* (*fum* to *succ*, blue) and for the reverse *b* → *a* (*succ* to *fum*, pink) transitions (overlapping regions are highlighted in purple). The boundaries *a* and *b*, indicated as dashed horizontal lines at the top, were chosen as half the mean position of *fum* and *succ* stations, respectively. The distributions are the same as determined by a two-sample Kolmogorov-Smirnov test (see Table S1). Scale bar: 1 s.

probabilities to move from one station to the other (or to any point *a* to point *b*) within a time interval ($P[a \rightarrow b, \Delta t]$ and $P[b \rightarrow a, \Delta t]$) informs on the Gibbs free energy change of the system (ΔG) following

$$\frac{P[a \rightarrow b, \Delta t]}{P[b \rightarrow a, \Delta t]} = exp\left(\frac{-\Delta G}{k_B T}\right), \qquad \text{(Equation 1)}$$

where k_B is the Boltzmann constant and T is temperature.

The identity between the LTFT times, although counterintuitive as it involves that the time the macrocycle takes to go uphill in energy is the same as it takes to go downhill, follows from microscopic reversibility. We used the mechanical equilibrium extension trajectories of individual molecular shuttles to experimentally test Equation 1 for calculating ΔG using transition probabilities from trajectory thermodynamics rather than state probability distributions (further details in supplemental information and Figure S24).[39] In addition, we compared the ΔG results (energy landscapes) obtained through this method with those obtained from position probabilities using the inverse Boltzmann's distribution method.[49] Equation 1 holds as long as the molecule is in mechanical equilibrium, i.e., the motion has a low Reynold's number, which is the case for all molecules in solution. In contrast, the Boltzmann equation $\frac{p_b}{p_a} = exp\left(\frac{-\Delta G}{k_B T}\right)$ for the probabilities of the system to be in the vicinity of point *b* relative to point *a* holds only at thermodynamic equilibrium, which is a considerably more stringent and less universal condition. In this case, both methods yielded comparable energy profile values across the whole spectrum of population distributions (Figure 4), thus confirming the applicability of this method to obtain thermodynamic variables from molecular-scale hopping experiments.

Conclusions

The recent application of single-molecule manipulation techniques in the field of supramolecular chemistry is allowing us to observe and characterize individual transition paths and the microscopic thermally driven motions that underlie the conformational changes occurring during operation of synthetic devices.[14] Microscopic reversibility is the organizing principle by which molecular machines can be understood.[50] Here, we experimentally demonstrated the ramifications of microscopic reversibility during the switching of the macrocycle of a molecular shuttle, which could be considered as a necessary first step to understand the operation of these devices. Our work opens a way to explore the properties of transition paths under nonequilibrium conditions, which will provide additional insight into the landscape not frequently visited in equilibrium and even the possibility of symmetry breaking (as recently shown in other systems).[34,51] The mechanical equilibrium transition probabilities enter into the nonequilibrium pumping equality for the nonequilibrium steady-state distribution $\frac{p_{b,ss}}{p_{a,ss}} = \frac{P[a \rightarrow b, \Delta t]}{P[b \rightarrow a, \Delta t]} \langle e^{\mathcal{W}_{\mathrm{pd}, \mathcal{S}_{a \rightarrow b}} / k_B T} \rangle$.[52] The term in angle brackets is the exponential of the path-dependent energy exchanged with the environment in the specific path $\mathcal{S}_{a \rightarrow b}$ kinetically weighted and averaged over all paths from *a* to *b*. It is in this term that all nonequilibrium aspects of a chemically driven nonequilibrium steady state are to be found (supplemental information and Figure S25). In addition, we will soon be able to examine the shape (extension vs. time) of the transition paths to retrieve information about the temporal sequence of events and investigate the possibility of taking multiple routes through the energy landscape. Comparison

Please cite this article in press as: Nicolás-García et al., Transition-path times of individual molecular shuttles under mechanical equilibrium show symmetry, Chem (2025), https://doi.org/10.1016/j.chempr.2024.102410

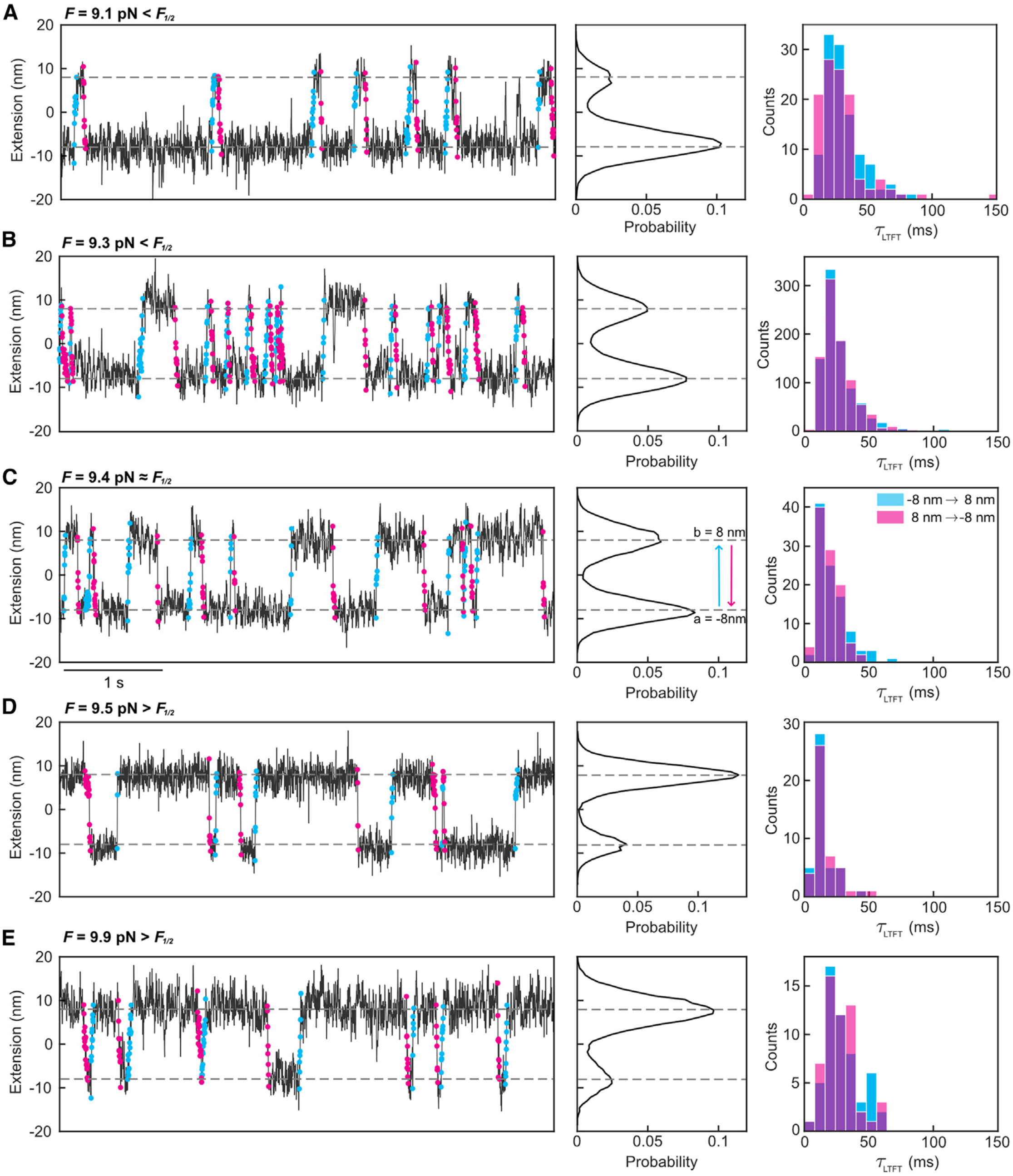

Figure 3. Calculation of LTFT time distributions from individual shuttling events recorded at different forces

Left, representative segments of extension vs. time traces recorded at various constant forces close to the coexistence force ($F_{1/2} \approx 9.4$ pN). Scale bar for all extension vs. time traces: 1 s. Data points corresponding to $a \rightarrow b$ and $b \rightarrow a$ transitions are represented as blue and pink dots, respectively. Central panels show the corresponding extension distributions. Right, the corresponding distributions of τ_{LTFT} showing symmetry between $a \rightarrow b$ (blue) and $b \rightarrow a$ (pink) transitions in all cases (overlapping regions are highlighted in purple), as concluded by Kolmogorov-Smirnov and Mann-Whitney significance tests (see Table S3). Dashed horizontal lines indicate the limits $a = -8$ nm and $b = 8$ nm in all plots.

of the transition-path shapes between molecular shuttles harboring different chemical components, or those of a single shuttle evaluated under different experimental conditions, will inform on the effect of these variables on the temporal sequence of events, the paths for crossing the energy barrier, and the thermodynamics of the shuttling motion at each condition. This information will be crucial in the design and optimization of molecular shuttling nanotechnology with improved properties. Finally, the combination of experimental information about transition paths with theory will help to characterize the fundamental features of the microscopic mechanisms of shuttling quantitatively.

Please cite this article in press as: Nicolás-García et al., Transition-path times of individual molecular shuttles under mechanical equilibrium show symmetry, Chem (2025), https://doi.org/10.1016/j.chempr.2024.102410

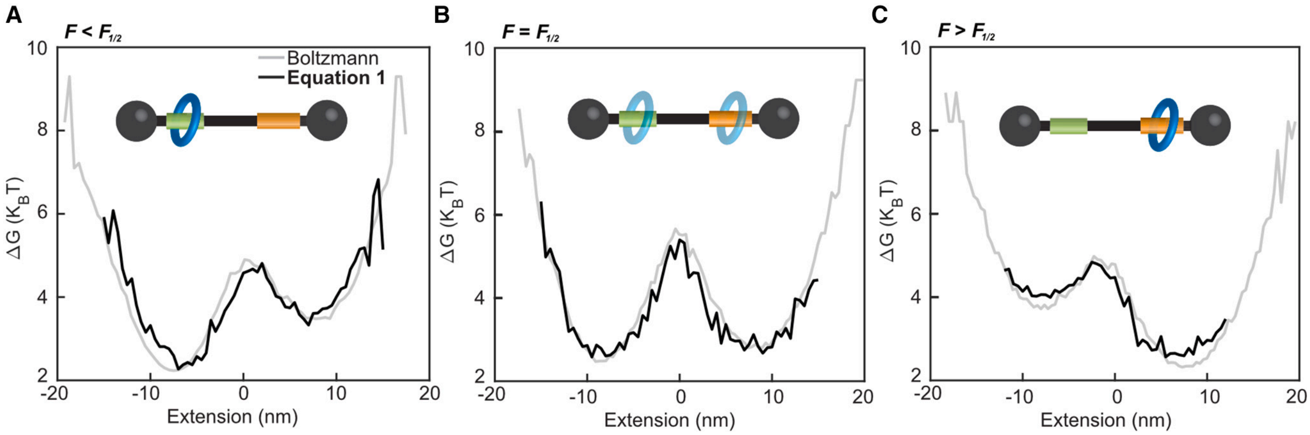

Figure 4. Energy landscapes calculated for individual molecular shuttles

Energy profiles at and near the coexistence force ($F_{1/2}$) obtained using the inverse Boltzmann's distribution method (gray lines) and Equation 1 (black lines) for (A) F = 9.3 pN, (B) $F_{1/2}$ = 9.4 pN, and (C) F = 9.9 pN. Both methods show comparable results.

METHODS

Further details regarding the methods can be found in the supplemental information.

RESOURCE AVAILABILITY

Lead contact

Further information and requests for resources should be directed to and will be fulfilled by the lead contact, Borja Ibarra (borja.ibarra@imdea.org).

Materials availability

The new compounds generated in this study require substantial time and resources for their preparation. Samples may be provided upon request pending their availability. Any request for advice to perform their synthesis following the protocols reported below is welcome.

Data and code availability

Analysis codes are freely available at https://hdl.handle.net/20.500.12614/3812. Raw data are available upon reasonable request to the lead contact, Borja Ibarra (borja.ibarra@imdea.org).

ACKNOWLEDGMENTS

This study was supported by MCIN/AEI/10.13039/501100011033 (grants PID2021-126755NB-I00, PID2020-116661RB-I00, and PGC2018-099341-B-I00); Comunidad de Madrid (NanoMagCOST P2018 INMT-4321 and P2018/NMT-4367 and MAD2D-CM-IMDEA); the Recovery, Transformation and Resilience Plan; and NextGenerationEU from the European Union. IMDEA Nanociencia receives support from the "Severo Ochoa" Programme for Centres of Excellence in R&D (MICINN, grant CEX2020-001039-S). T.N.-G. was supported by the MINECO (BES-2017-082582). N.M.S. acknowledges the MSCA program MSCA-IF-2019-892667.

AUTHOR CONTRIBUTIONS

T.N.-G. conducted the synthesis and characterization of compounds. T.N.-G. and R.B. conducted the optical tweezers single-molecule experiments. N.M.S. performed the data analysis. T.N.-G. performed the DFT calculations. B.I. and E.M.P. designed the experiments and directed the research. R.D.A., B.I., and E.M.P. supervised the experiments and data analysis. All authors contributed to the analysis of the results. T.N.-G., N.M.S., B.I., and E.M.P. prepared the initial manuscript and wrote the article with comments from all the authors.

DECLARATION OF INTERESTS

The authors declare no competing interests.

SUPPLEMENTAL INFORMATION

Supplemental information can be found online at https://doi.org/10.1016/j.chempr.2024.102410.

Received: July 26, 2024
Revised: September 6, 2024
Accepted: December 31, 2024
Published: February 11, 2025

REFERENCES

1. Kay, E.R., Leigh, D.A., and Zerbetto, F. (2007). Synthetic Molecular Motors and Mechanical Machines. Angew. Chem. Int. Ed. Engl. *46*, 72–191. https://doi.org/10.1002/anie.200504313.
2. Pezzato, C., Cheng, C., Stoddart, J.F., and Astumian, R.D. (2017). Mastering the non-equilibrium assembly and operation of molecular machines. Chem. Soc. Rev. *46*, 5491–5507. https://doi.org/10.1039/C7CS00068E.
3. Neupane, K., Foster, D.A.N., Dee, D.R., Yu, H., Wang, F., and Woodside, M.T. (2016). Direct observation of transition paths during the folding of proteins and nucleic acids. Science *352*, 239–242. https://doi.org/10.1126/science.aad0637.
4. Neupane, K., Wang, F., and Woodside, M.T. (2017). Direct measurement of sequence-dependent transition path times and conformational diffusion in DNA duplex formation. Proc. Natl. Acad. Sci. USA *114*, 1329–1334. https://doi.org/10.1073/pnas.1611602114.
5. Yu, H., Dee, D.R., Liu, X., Brigley, A.M., Sosova, I., and Woodside, M.T. (2015). Protein misfolding occurs by slow diffusion across multiple barriers in a rough energy landscape. Proc. Natl. Acad. Sci. USA *112*, 8308–8313. https://doi.org/10.1073/pnas.1419197112.
6. Hoffer, N.Q., and Woodside, M.T. (2019). Probing microscopic conformational dynamics in folding reactions by measuring transition paths. Curr. Opin. Chem. Biol. *53*, 68–74. https://doi.org/10.1016/j.cbpa.2019.07.006.

7. Chung, H.S., McHale, K., Louis, J.M., and Eaton, W.A. (2012). Single-Molecule Fluorescence Experiments Determine Protein Folding Transition Path Times. Science *335*, 981–984. https://doi.org/10.1126/science.1215768.

8. Stoddart, J.F. (2017). Mechanically Interlocked Molecules (MIMs)—Molecular Shuttles, Switches, and Machines (Nobel Lecture). Angew. Chem. Int. Ed. Engl. *56*, 11094–11125. https://doi.org/10.1002/anie.201703216.

9. Sauvage, J.-P. (2017). From Chemical Topology to Molecular Machines (Nobel Lecture). Angew. Chem. Int. Ed. Engl. *56*, 11080–11093.

10. Bissell, R.A., Córdova, E., Kaifer, A.E., and Stoddart, J.F. (1994). A chemically and electrochemically switchable molecular shuttle. Nature *369*, 133–137. https://doi.org/10.1038/369133a0.

11. Berná, J., Leigh, D.A., Lubomska, M., Mendoza, S.M., Pérez, E.M., Rudolf, P., Teobaldi, G., and Zerbetto, F. (2005). Macroscopic transport by synthetic molecular machines. Nat. Mater. *4*, 704–710. https://doi.org/10.1038/nmat1455.

12. Martinez-Cuezva, A., Saura-Sanmartin, A., Nicolas-Garcia, T., Navarro, C., Orenes, R.A., Alajarin, M., and Berna, J. (2017). Photoswitchable interlocked thiodiglycolamide as a cocatalyst of a chalcogeno-Baylis-Hillman reaction. Chem. Sci. *8*, 3775–3780. https://doi.org/10.1039/c7sc00724h.

13. Saura-Sanmartin, A., Nicolas-Garcia, T., Pastor, A., Quiñonero, D., Alajarin, M., Martinez-Cuezva, A., and Berna, J. (2023). Control of the assembly of a cyclic hetero[4]pseudorotaxane from a self-complementary [2]rotaxane. Chem. Sci. *14*, 4143–4151. https://doi.org/10.1039/D3SC00886J.

14. Erbas-Cakmak, S., Fielden, S.D.P., Karaca, U., Leigh, D.A., McTernan, C.T., Tetlow, D.J., and Wilson, M.R. (2017). Rotary and linear molecular motors driven by pulses of a chemical fuel. Science *358*, 340–343. https://doi.org/10.1126/science.aao1377.

15. Sluysmans, D., Devaux, F., Bruns, C.J., Stoddart, J.F., and Duwez, A.-S. (2018). Dynamic force spectroscopy of synthetic oligorotaxane foldamers. Proc. Natl. Acad. Sci. USA *115*, 9362–9366. https://doi.org/10.1073/pnas.1712790115.

16. Collier, C.P., Wong, E.W., Belohradský, M., Raymo, F.M., Stoddart, J.F., Kuekes, P.J., Williams, R.S., and Heath, J.R. (1999). Electronically Configurable Molecular-Based Logic Gates. Science *285*, 391–394. https://doi.org/10.1126/science.285.5426.391.

17. Green, J.E., Wook Choi, J., Boukai, A., Bunimovich, Y., Johnston-Halperin, E., DeIonno, E., Luo, Y., Sheriff, B.A., Xu, K., Shik Shin, Y., et al. (2007). A 160-kilobit molecular electronic memory patterned at 1011 bits per square centimetre. Nature *445*, 414–417. https://doi.org/10.1038/nature05462.

18. Lewandowski, B., De Bo, G., Ward, J.W., Papmeyer, M., Kuschel, S., Aldegunde, M.J., Gramlich, P.M.E., Heckmann, D., Goldup, S.M., D'Souza, D.M., et al. (2013). Sequence-specific peptide synthesis by an artificial small-molecule machine. Science *339*, 189–193. https://doi.org/10.1126/science.1229753.

19. Chen, L., Nixon, R., and De Bo, G. (2024). Force-controlled release of small molecules with a rotaxane actuator. Nature *628*, 320–325. https://doi.org/10.1038/s41586-024-07154-0.

20. Astumian, R.D. (2018). Stochastic pumping of non-equilibrium steady-states: how molecules adapt to a fluctuating environment. Chem. Commun. *54*, 427–444. https://doi.org/10.1039/C7CC06683J.

21. Leanza, L., Perego, C., Pesce, L., Salvalaglio, M., von Delius, M., and Pavan, G.M. (2023). Into the dynamics of rotaxanes at atomistic resolution. Chem. Sci. *14*, 6716–6729. https://doi.org/10.1039/D3SC01593A.

22. Panman, M.R., Bodis, P., Shaw, D.J., Bakker, B.H., Newton, A.C., Kay, E.R., Brouwer, A.M., Buma, W.J., Leigh, D.A., and Woutersen, S. (2010). Operation Mechanism of a Molecular Machine Revealed Using Time-Resolved Vibrational Spectroscopy. Science *328*, 1255–1258. https://doi.org/10.1126/science.1187967.

23. Garaudée, S., Silvi, S., Venturi, M., Credi, A., Flood, A.H., and Stoddart, J.F. (2005). Shuttling Dynamics in an Acid–Base-Switchable [2]Rotaxane. ChemPhysChem *6*, 2145–2152. https://doi.org/10.1002/cphc.200500295.

24. Lane, A.S., Leigh, D.A., and Murphy, A. (1997). Peptide-Based Molecular Shuttles. J. Am. Chem. Soc. *119*, 11092–11093. https://doi.org/10.1021/ja971224t.

25. Collin, J.-P., Durola, F., Lux, J., and Sauvage, J.-P. (2009). A Rapidly Shuttling Copper-Complexed [2]Rotaxane with Three Different Chelating Groups in Its Axis. Angew. Chem. Int. Ed. Engl. *48*, 8532–8535. https://doi.org/10.1002/anie.200903311.

26. Brough, B., Northrop, B.H., Schmidt, J.J., Tseng, H.-R., Houk, K.N., Stoddart, J.F., and Ho, C.-M. (2006). Evaluation of synthetic linear motor-molecule actuation energetics. Proc. Natl. Acad. Sci. USA *103*, 8583–8588. https://doi.org/10.1073/pnas.0509645103.

27. Shigekawa, H., Miyake, K., Sumaoka, J., Harada, A., and Komiyama, M. (2000). The Molecular Abacus: STM Manipulation of Cyclodextrin Necklace. J. Am. Chem. Soc. *122*, 5411–5412. https://doi.org/10.1021/ja000037j.

28. Chen, S., Su, D., Jia, C., Li, Y., Li, X., Guo, X., Leigh, D.A., and Zhang, L. (2022). Real-time observation of the dynamics of an individual rotaxane molecular shuttle using a single-molecule junction. Chem *8*, 243–252. https://doi.org/10.1016/j.chempr.2021.11.012.

29. Zhang, Z.-H., Feng, H.-N., Chi, G., Leigh, D.A., and Zhang, L. (2023). Single-Molecule Studies on Artificial Small-Molecule Machines. CCS Chem. *5*, 2448–2465. https://doi.org/10.31635/ccschem.023.202302949.

30. Lussis, P., Svaldo-Lanero, T., Bertocco, A., Fustin, C.A., Leigh, D.A., and Duwez, A.S. (2011). A single synthetic small molecule that generates force against a load. Nat. Nanotechnol. *6*, 553–557. https://doi.org/10.1038/nnano.2011.132.

31. Sluysmans, D., Hubert, S., Bruns, C.J., Zhu, Z., Stoddart, J.F., and Duwez, A.-S. (2018). Synthetic oligorotaxanes exert high forces when folding under mechanical load. Nat. Nanotechnol. *13*, 209–213. https://doi.org/10.1038/s41565-017-0033-7.

32. Sluysmans, D., Lussis, P., Fustin, C.A., Bertocco, A., Leigh, D.A., and Duwez, A.S. (2021). Real-Time Fluctuations in Single-Molecule Rotaxane Experiments Reveal an Intermediate Weak Binding State during Shuttling. J. Am. Chem. Soc. *143*, 2348–2352. https://doi.org/10.1021/jacs.0c12161.

33. Neupane, K., Hoffer, N.Q., and Woodside, M.T. (2018). Measuring the Local Velocity along Transition Paths during the Folding of Single Biological Molecules. Phys. Rev. Lett. *121*, 018102. https://doi.org/10.1103/PhysRevLett.121.018102.

34. Gladrow, J., Ribezzi-Crivellari, M., Ritort, F., and Keyser, U.F. (2019). Experimental evidence of symmetry breaking of transition-path times. Nat. Commun. *10*, 55. https://doi.org/10.1038/s41467-018-07873-9.

35. Naranjo, T., Lemishko, K.M., de Lorenzo, S., Somoza, Á., Ritort, F., Pérez, E.M., and Ibarra, B. (2018). Dynamics of individual molecular shuttles under mechanical force. Nat. Commun. *9*, 4512. https://doi.org/10.1038/s41467-018-06905-8.

36. Bier, M., Derényi, I., Kostur, M., and Astumian, R.D. (1999). Intrawell relaxation of overdamped Brownian particles. Phys. Rev. E Stat. Phys. Plasmas Fluids Relat. Interdiscip. Topics *59*, 6422–6432. https://doi.org/10.1103/PhysRevE.59.6422.

37. Astumian, R.D., and Bier, M. (1994). Fluctuation driven ratchets: Molecular motors. Phys. Rev. Lett. *72*, 1766–1769. https://doi.org/10.1103/PhysRevLett.72.1766.

38. Derényi, I., and Astumian, R.D. (1999). Intrawell Relaxation Time: The Limit of the Adiabatic Approximation. Phys. Rev. Lett. *82*, 2623–2627. https://doi.org/10.1103/PhysRevLett.82.2623.

39. Confesor, M.N.P. (2015). Bier-Astumian relation, fluctuation theorem and their possible applications. Int. J. Mod. Phys. Conf. Ser. *36*, 1560009. https://doi.org/10.1142/S2010194515600095.

40. Berná, J., Bottari, G., Leigh, D.A., and Pérez, E.M. (2007). Amide-based molecular shuttles (2001–2006). Pure Appl. Chem. *79*, 39–54. https://doi.org/10.1351/pac200779010039.
41. Altieri, A., Bottari, G., Dehez, F., Leigh, D.A., Wong, J.K.Y., and Zerbetto, F. (2003). Remarkable Positional Discrimination in Bistable Light- and Heat-Switchable Hydrogen-Bonded Molecular Shuttles. Angew. Chem. Int. Ed. Engl. *42*, 2296–2300. https://doi.org/10.1002/anie.200250745.
42. Chaudhury, S., and Makarov, D.E. (2010). A harmonic transition state approximation for the duration of reactive events in complex molecular rearrangements. J. Chem. Phys. *133*, 034118. https://doi.org/10.1063/1.3459058.
43. Onsager, L., and Machlup, S. (1953). Fluctuations and Irreversible Processes. Phys. Rev. *91*, 1505–1512. https://doi.org/10.1103/PhysRev.91.1505.
44. Berezhkovskii, A.M., Hummer, G., and Bezrukov, S.M. (2006). Identity of Distributions of Direct Uphill and Downhill Translocation Times for Particles Traversing Membrane Channels. Phys. Rev. Lett. *97*, 020601. https://doi.org/10.1103/PhysRevLett.97.020601.
45. Kamenev, A. (2011). Field Theory of Non-Equilibrium Systems (Cambridge University Press). https://doi.org/10.1017/CBO9781139003667.
46. Hummer, G. (2004). From transition paths to transition states and rate coefficients. J. Chem. Phys. *120*, 516–523. https://doi.org/10.1063/1.1630572.
47. Astumian, R.D., and Brody, R. (2009). Thermodynamics of Gradient Driven Transport: Application to Single-Particle Tracking. J. Phys. Chem. B *113*, 11459–11462. https://doi.org/10.1021/jp903746j.
48. Purcell, E.M. (1977). Life at low Reynolds number. Am. J. Phys. *45*, 3–11. https://doi.org/10.1119/1.10903.
49. Woodside, M.T., Anthony, P.C., Behnke-Parks, W.M., Larizadeh, K., Herschlag, D., and Block, S.M. (2006). Direct Measurement of the Full, Sequence-Dependent Folding Landscape of a Nucleic Acid. Science *314*, 1001–1004. https://doi.org/10.1126/science.1133601.
50. Astumian, R.D. (2012). Microscopic reversibility as the organizing principle of molecular machines. Nat. Nanotechnol. *7*, 684–688. https://doi.org/10.1038/nnano.2012.188.
51. Binks, L., Borsley, S., Gingrich, T.R., Leigh, D.A., Penocchio, E., and Roberts, B.M.W. (2023). The role of kinetic asymmetry and power strokes in an information ratchet. Chem *9*, 2902–2917. https://doi.org/10.1016/j.chempr.2023.05.035.
52. Astumian, R.D., and Robertson, B. (1993). Imposed oscillations of kinetic barriers can cause an enzyme to drive a chemical reaction away from equilibrium. J. Am. Chem. Soc. *115*, 11063–11068. https://doi.org/10.1021/ja00077a001.

Chem, Volume *11*

Supplemental information

Transition-path times of individual molecular shuttles under mechanical equilibrium show symmetry

Tomás Nicolás-García, Natalia Martín Sabanés, Rebeca Bocanegra, R. Dean Astumian, Emilio M. Pérez, and Borja Ibarra

SUPPLEMENTAL METHODS

Table of contents

1. General methodology.

All solvents were dried according to standard procedures. Reagents were used as purchased. All air-sensitive reactions were carried out under inert atmosphere. DNA oligonucleotides were purchased from Biomers. Column chromatography was carried out using silica gel (Merck, Kieselgel 60, 230-240 mesh) as a stationary phase. Analytical thin layer chromatography (TLC) was performed on precoated silica gel on aluminum cards (0.25 mm thick, with fluorescent indicator 254 nm) and observed under UV light. NMR spectra were recorded on a BrukerAvance 400 (^{1}H: 400 MHz; ^{13}C: 101 MHz) spectrometer at 298 K using partially deuterated solvents as internal standards, unless otherwise stated. Spectra of the synthesized compounds were assigned with the aid of both DEPT and 2D NMR experiments (COSY, HMQC or HMBC). Coupling constants (*J*) are expressed in Hz and chemical shifts (δ) in ppm. Multiplicities are denoted as follows: s = singlet; br = broad; d = doublet; t = triplet; m = multiplet. High-Resolution Mass Spectroscopy (HRMS) was obtained using both Atmospheric-Pressure Chemical Ionization (APCI) and Electrospray Ionization (ESI) on a MAXIS II (Bruker) spectrometer, Matrix-Assisted Laser Desorption Ionization (MALDI-TOF) on a VS AutoSpec spectrometer, both coupled to a time-of-flight (TOF) instrument and time-of-flight mass spectrometry coupled to a Gas Chromatograph with Electron Ionization (GCEI) on a GCT Agilent Technologies 6890N. UV-Vis spectroscopy was performed on a Cary 50 UV-Visible spectrophotometer. Fourier-transform infrared spectroscopy with attenuated total reflection (FT-ATR-IR) was performed on a Bruker ALPHA FTIR spectrometer. The conditions used for all the collected data were: 24 scans, 24 seconds each experiment, transmission mode.

<u>Abbreviation list:</u>

DBU: Diazabicycloundecene

DCM: Dichloromethane

DFT: Density functional theory

DMAP: 4-Dimethylaminopyridine

DMF: *N,N*-dimethylformamide

EDCI·HCl: *N*-(3-dimethylaminopropyl)-*N*'-ethylcarbodiimide hydrochloride

LTFT: Last touch first touch times

NMR: Nuclear Magnetic Resonance Spectroscopy

PEG: Polyethylene glycol

TFA: Trifluoroacetic acid

THF: Tetrahydrofuran

TLC: Thin Layer Chromatography

WLC: Worm-like chain (model)

2. Synthesis of molecular shuttle 15.

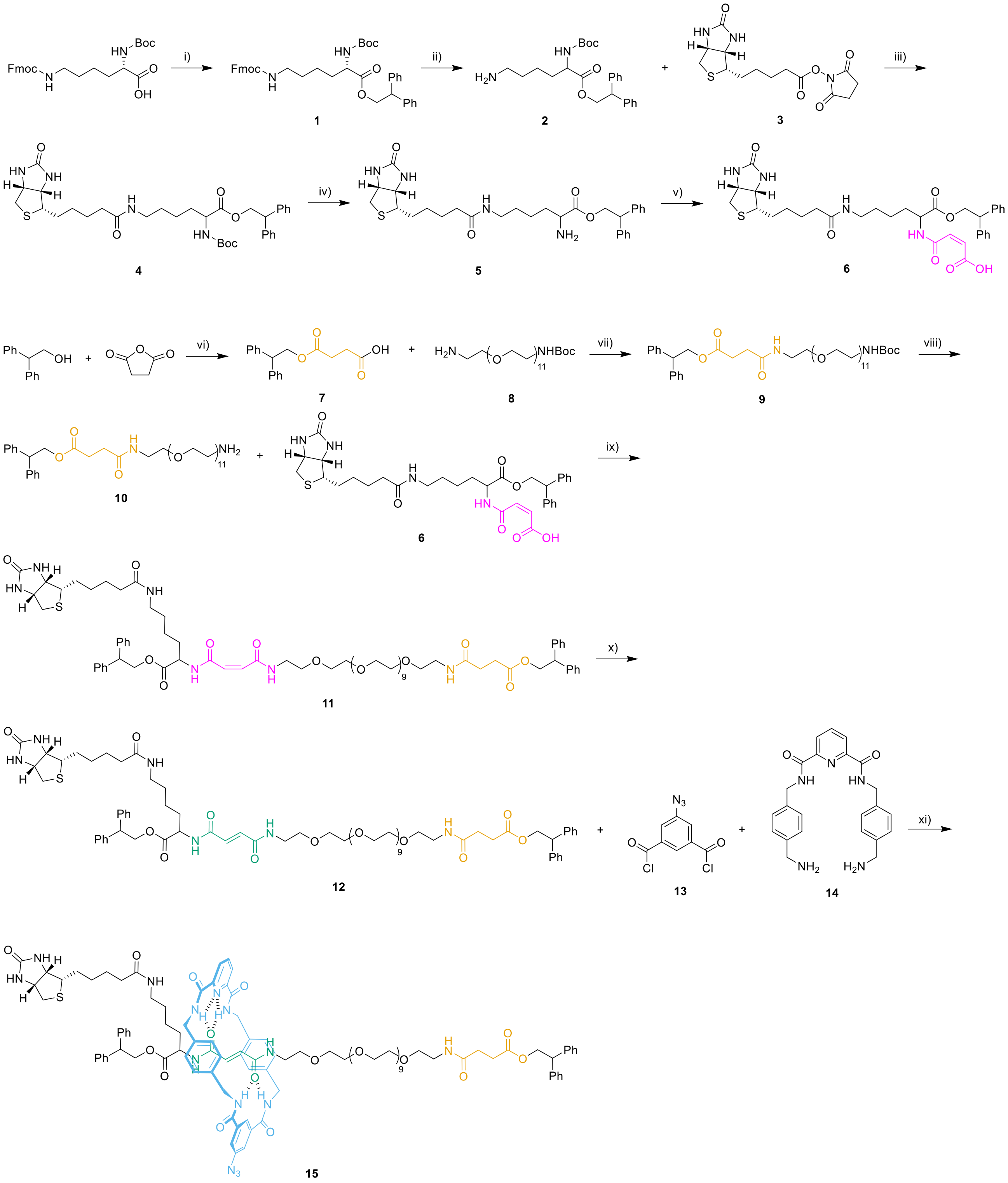

Figure S1: Preparation of molecular shuttle 15. Reagents and conditions: i) 2,2-diphenylethanol, DMAP, EDCI·HCl, DCM, 0 ºC to r.t. 12 h, 99%; ii) piperidine, DBU, DMF, r.t. 4 h, 99%; iii) Et_3N, DMF, 0 ºC to r.t. 12 h, 96%; iv) TFA, DCM, 0 ºC to r.t. 4 h, 99%; v) maleic anhydride, Et_3N, THF, 0 ºC to r.t. 12 h, 90%; vi) Et_3N, DCM, 12h, 76%; vii) EDCI·HCl, DMAP, DCM, 0 ºC to r.t. 12 h, 90%; viii) TFA, DCM, 0 ºC to r.t. 4 h, 99%; ix) EDCI·HCl, DMAP, DCM, 0 ºC to r.t. 12 h, 60%; x) Piperidine, DCM, 48 h, 97%; xi) Et_3N, $CHCl_3$, r.t. 12 h, 46%.

Compound 1

To a solution of Boc-D-Lys(Fmoc)-OH (900 mg, 1.92 mmol) in dry DCM (25 mL) under N_2 atmosphere, diphenylethanol (457 mg, 2.3 mmol) and a catalytic amount of DMAP were added and the mixture was stirred at 0 ºC for 5 minutes. Afterwards, EDCI·HCl (732 mg, 3.84 mmol) was added at 0 ºC and the reaction mixture was stirred at room temperature overnight. The reaction mixture was concentrated under reduced pressure and then diluted with DCM. Next, the mixture was washed with 1 M HCl (2 x 100 mL), $NaHCO_3$ (sat. aq.) (2 x 100 mL) and brine (1 x 100 mL). The organic layers were dried over anhydrous $MgSO_4$ and concentrated under reduced pressure. The crude was purified by column chromatography on silica gel using a hexane/EtOAc 75/25 mixture as eluent, to furnish compound **1** as colorless oil (1.12 g, 99%). Its spectroscopic data were in concordance with those described in bibliography.[S1]

Compound 2

Compound **1** (90 mg, 0.14 mmol) was dissolved in 1% piperidine and 1% DBU in DMF (2.8 mL). The reaction mixture was stirred for 3 hours at room temperature until the Fmoc deprotection was completed (followed by TLC). The solvent was removed under reduced pressure to give compound **2** as yellowish oil (assumed quantitative yield), and the crude material was used in the next step reaction without further purification. Its spectroscopic data were in concordance with those described in bibliography.[S1]

Compound 3

EDCI·HCl (71 mg, 0.37 mmol) was added to a solution of D-biotin (75 mg, 0.31 mmol) and *N*-hydroxysuccinimide (39 mg, 0.34 mmol) in DMF at 0 ºC. The reaction mixture was stirred at room temperature for 24 hours. Afterwards, solvent was removed to obtain a solid. Finally, the solid was washed several times with methanol to furnish compound **3** as a white solid (96 mg, 90%). Its spectroscopic data were in concordance with those described in bibliography.[S1]

Compound 4

Compounds **2** (46 mg, 0.110 mmol), **3** (25 mg, 0.073 mmol), and 2 drops of Et_3N were dissolved in DMF (5 mL) and the reaction mixture was stirred overnight. Afterwards, the residue was diluted in DCM and washed by water. The organic phase was dried over anhydrous $MgSO_4$ and concentrated under reduced pressure. The crude was purified by column chromatography on silica gel using a gradient elution, from $CHCl_3$ to $CHCl_3$/MeOH 90/10, to furnish compound **4** as colorless oil (45 mg, 96%). Its spectroscopic data were in concordance with those described in bibliography.[S1]

Compound 5

To a solution of compound **4** (120 mg, 0.19 mmol) in DCM (2 mL) TFA (0.30 mL, 4.00 mmol) was added dropwise at 0 ºC. The reaction was stirred at room temperature for 4 hours until it was completed (followed by TLC). Then, the solvent and excess of TFA were removed under reduced pressure and the crude was dissolved in a mixture DCM/MeOH 1/1 and Amberlyst® A21 was added. The mixture was stirred at room temperature for 1 hour. Afterwards, the mixture was filtered off, and the solvent was removed under reduced pressure, to furnish the unprotected amine **5**, which was used in the next step without further purification. Its spectroscopic data were in concordance with those described in bibliography.[S1]

Compound 6

Compound **5** (49 mg, 0.09 mmol) and 1 drop of Et_3N were dissolved in dry THF (1 mL) at 0 ºC, then maleic anhydride (9 mg, 0.093 mmol) dissolved in dry THF (0.4 mL) was dropwise added under inert atmosphere and the mixture was stirred at room temperature overnight. Afterwards, the solvent was removed under reduced pressure. The crude was purified by column chromatography on silica gel using a gradient elution, from DCM to DCM/MeOH 90/10 to DCM/MeOH/NH_3 80/20/0.2, to furnish compound **6** as yellowish oil (59 mg, 90%). Its spectroscopic data were in concordance with those described in bibliography.[S1]

Compound 7

2,2-diphenylethanol (1 g, 5.26 mmol) and 1 drop of Et_3N were dissolved in dry DCM (53 mL) and a solution of succinic anhydride (584 mg, 5.83 mmol) in DCM (15 mL) was added dropwise for 30 minutes and the mixture was stirred at room temperature overnight. Afterwards, the solvent was removed under reduced pressure. The crude was purified by column chromatography on silica gel using a hexane/EtOAc 70/30 mixture as eluent, to furnish the compound **7** as white solid (1.2 g, 76%). Its spectroscopic data were in concordance with those described in bibliography.[S1]

Compound 9

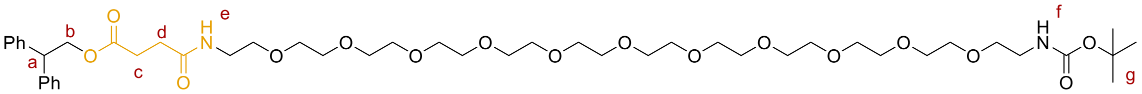

To a suspension of carboxylic acid **7** (57 mg, 0.19 mmol) in anhydrous DCM (2 mL) under N_2 atmosphere, commercially sourced O-(2-aminoethyl)-O′-[2-(Boc-amino)ethyl]decaethylene glycol (**8**, 100 mg, 0.15 mmol) and DMAP (25 mg, 0.20 mmol) were added, and the solution was stirred at 0 ºC for 10 minutes. Afterwards, EDCI·HCl (40 mg, 0.20 mmol) was added at 0 ºC and the reaction was stirred at room temperature for 24 hours. Next, the mixture was washed with 1 M HCl (2 x 100 mL), $NaHCO_3$ (sat. aq.) (2 x 100 mL) and brine (1 x 100 mL). The organic phases were dried over anhydrous $MgSO_4$ and concentrated under reduced pressure. The crude was purified by column chromatography on silica gel using a $CHCl_3$/MeOH 95/5 mixture as eluent, to give compound **9** as yellowish oil (125 mg, 90%). ^{1}H NMR (400 MHz, $CDCl_3$, 298 K) δ = 7.34 – 7.14 (m, 10H, Ar-H), 6.33 (br, 1H, NH_e), 5.11 (br, 1H, NH_f), 4.62 (d, *J* = 7.6 Hz, 2H, H_b), 4.35 (t, *J* = 7.6 Hz, 1H, H_a), 3.63 (m, *J* = 5.6 Hz, 40H, PEG-H), 3.51 (m, 4H, PEG-H), 3.40 (m, 2H, PEG-H), 3.30 (m, 2H, PEG-H), 2.56 (t, *J* = 7.0 Hz, 2H, H_c), 2.37 (t, *J* = 7.0 Hz, 2H, H_d), 1.44 (s, 9H, H_g). ^{13}C NMR (100 MHz, $CDCl_3$, 298 K) δ = 172.7 (C=O), 171.3 (C=O), 156.0 (C=O), 141.1 (C), 128.6 (CH), 128.2 (CH), 126.8 (CH), 79.1 (CH_2), 70.6 (CH_2), 70.2 (CH_2), 69.8 (CH_2), 66.8 (CH_2), 49.8 (CH), 40.4 (CH_2), 39.3 (CH_2), 30.7 (CH_2), 29.5 (CH_2), 28.5 (CH). HRMS (APCI) calculated for $C_{47}H_{77}N_2O_{16}$ $[M+H]^+$ 925.5268, found 925.5244.

Compound 10

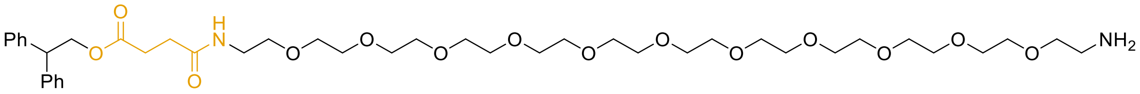

To a solution of compound **9** (110 mg, 0.12 mmol) in DCM (2 mL) TFA (0.30 mL, 4.00 mmol) was added dropwise at 0 ºC. The reaction was stirred at room temperature for 4 hours until it was completed (followed by TLC). Then, the solvent and excess of TFA were removed under reduced pressure and the crude was dissolved in a mixture DCM/MeOH 1/1 and Amberlyst® A21 was added. The mixture was stirred at room temperature for 1 hour. Afterwards, the resin was filtered, and the solvent was removed under reduced pressure, to give the unprotected amine **10**, which was used in the next step without further purification.

Thread 11

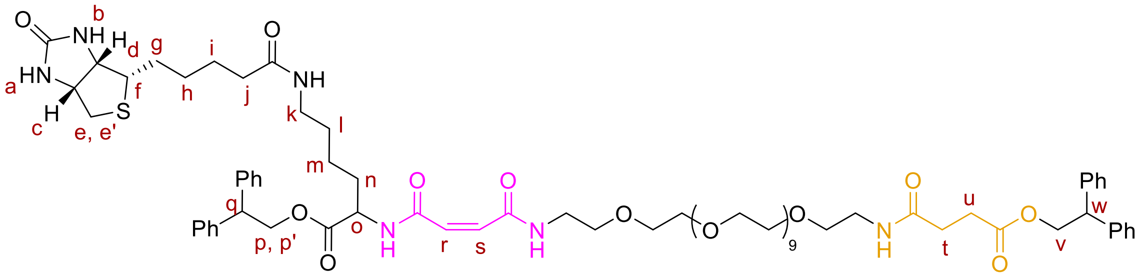

To a suspension of carboxylic acid **6** (85 mg, 0.13 mmol) in dry DCM (10 mL) under N_2 atmosphere, the amine **10** (107 mg, 0.12 mmol) and DMAP (23 mg, 0.19 mmol) were added, and the solution was stirred at 0 ºC for 5 minutes. Afterwards, EDCI·HCl (37 mg, 0.19 mmol) was added at 0 ºC and the reaction was stirred at room temperature for 24 hours. Next, the mixture was washed with 1 M HCl (2 x 100 mL), $NaHCO_3$ (sat. aq.) (2 x 100 mL) and brine (1 x 100 mL). The organic phase was dried over anhydrous $MgSO_4$ and concentrated under reduced pressure. The crude was purified by column chromatography on silica gel using a gradient elution, from DCM/MeOH 95/5 to 90/10, to give (*Z*/*E* 55/45)-thread **11** as colourless oil (112 mg, 60%). ^{1}H NMR (400 MHz, DMSO-d_6, 298 K) δ = 9.79 (d, *J* = 7.0 Hz, 0.5H, NH-*Z*-isomer), 9.06 (t, *J* = 5.6 Hz, 0.5H, NH-*Z*-isomer), 8.66 (d, *J* = 7.1 Hz, 0.5H, NH-*E*-isomer), 8.50 (t, *J* = 5.7 Hz, 0.5H, NH-*E*-isomer), 7.87 (t, *J* = 5.6 Hz, 1H, NH), 7.70 (m, *J* = 4.7 Hz, 1H, NH), 7.41 – 7.24 (m, 16H, Ar), 7.26 – 7.13 (m, 4H, Ar), 6.87 (d, *J* = 15.2 Hz, 0.4 H, H_r or H_s of *E*-isomer), 6.82 (d, *J* = 15.2 Hz, 0.4 H, H_r or H_s of *E*-isomer), 6.41 (br, 1 H, H_a), 6.34 (br, 1 H, H_b), 6.21 (d, *J* = 13.1 Hz, 0.5 H, H_r or H_s of *Z*-isomer), 6.07 (d, *J* = 13.1 Hz, 0.5 H, H_r or H_s of *Z*-isomer), 4.73 (dd, *J* = 10.7, 8.2 Hz, 1H, H_p or $H_{p'}$), 4.56 (m, 3H, $H_{p'}$ or H_p, H_v), 4.43 – 4.22 (m, 3H, H_c, H_q, H_w), 4.12 (m, 2H, H_d, H_o), 3.50 (m, 44H, PEG-H), 3.37 (t, *J* = 5.9 Hz, 2H, PEG-H), 3.16 (dd, *J* = 11.5, 5.8, Hz, 2H, PEG-H), 3.08 (m, 1H, H_f), 2.91 (m, 2H, H_k), 2.81 (dd, *J* = 12.4, 5.1 Hz, 1H, H_e or $H_{e'}$), 2.60 (d, J = 14.1 Hz, 1 H, He´ or He), 2.37 (t, *J* = 7.0 Hz, 2H, H_u), 2.27 (t, *J* = 6.7 Hz, 2H, H_t), 2.04 (t, *J* = 7.4 Hz, 2H, H_j), 1.68 – 1.09 (m, 12H, $H_{g+h+i+l+m+n}$). ^{13}C NMR (100 MHz, DMSO-*d*$_6$, 298 K) δ = 172.3 (C=O), 171.8 (C=O), 171.5 (C=O), 170.6 (C=O), 162.7 (C=O), 141.5 (C), 141.3 (C), 141.2 (C), 128.5 (CH), 128.0 (CH), 126.6 (CH), 69.8 (CH_2), 69.6 (CH_2), 69.1 (CH_2), 66.4 (CH_2),66.0 (CH_2), 61.0 (CH), 59.2 (CH), 55.4 (CH), 49.2 (CH_2), 35.2 (CH_2), 29.6 (CH_2), 28.9 (CH_2), 28.8 (CH_2), 28.2 (CH_2), 28.0 (CH_2), 25.3 (CH_2). HRMS (APCI) calculated for $C_{76}H_{109}N_6O_{20}S$ $[M+H]^+$ 1457.7412, found 1457.7401.

Thread 12

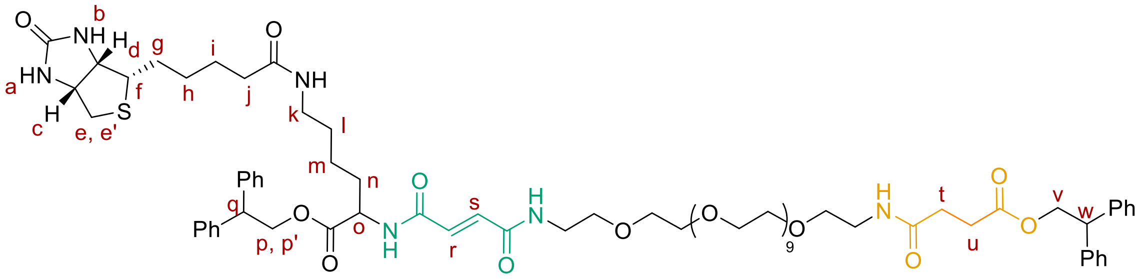

A solution of **11** (63 mg, 0.043 mmol) and 3 drops of piperidine in dry DCM (3 mL) was stirred at room temperature for 48 hours. Then, DCM was added, and the organic layer was washed twice with HCl 1 M and dried over anhydrous $MgSO_4$ and concentrated under reduced pressure to give thread **12** as yellowish oil (61 mg, 97%). ^{1}H NMR (400 MHz, DMSO-*d*$_6$, 298 K) δ = 8.66 (d, *J* = 7.2 Hz, 1H, NH), 8.51 (t, *J* = 5.7 Hz, 1H, NH), 7.87 (t, *J* = 5.5 Hz, 1H, NH), 7.71 (t, *J* = 5.3 Hz, 1H NH), 7.38 – 7.27 (m, 16H), 7.21 (m, 4H), 6.87 (d, *J* = 15.3 Hz, 1H, H_r or H_s), 6.82 (d, *J* = 15.3 Hz, 1H, H_s or H_r), 6.41 (br, 1H, H_a), 6.34 (br, 1H, H_b), 4.72 (dd, *J* = 10.9, 8.1 Hz, 1H, H_p or $H_{p'}$), 4.55 (m, 3H, $H_{p'}$ or H_p, H_v), 4.33 (m, 3H, H_c, H_q, H_w), 4.13 (m, 2H, H_d, H_o), 3.58 – 3.42 (m, 44H, PEG-H), 3.37 (t, *J* = 5.9 Hz, 2H, PEG-H), 3.17 (dd, *J* = 11.5, 5.9 Hz, 2H, PEG-H), 3.09 (m, 1H, H_f), 2.91 (m, 2H, H_k), 2.81 (dd, *J* =12.4, 5.1 Hz, 1H, H_e or $H_{e'}$), 2.57 (d, *J* = 12.4 Hz, 1H, $H_{e'}$ or H_e), 2.37 (t, *J* = 6.8 Hz, 2H, H_u), 2.27 (t, *J* = 6.8 Hz, 2H, H_t), 2.04 (t, *J* = 6.8 Hz, 2H, H_j), 1.68 – 1.09 (m, 12H, $H_{g+h+i+l+m+n}$). ^{13}C NMR (100 MHz, DMSO-*d*$_6$, 298 K) δ = 172.3 (C=O), 171.8 (C=O), 171.6 (C=O), 170.6 (C=O), 163.8 (C=O), 163.7 (C=O), 162.7 (C=O), 141.5 (C), 141.3 (C), 141.2 (C), 128.5 (CH), 127.9 (CH), 126.6 (CH), 69.8 (CH_2), 69.6 (CH_2), 69.1 (CH_2), 68.9 (CH_2), 66.4 (CH_2), 66.0 (CH_2), 61.0 (CH), 59.2 (CH), 55.4 (CH), 52.3 (CH_2), 49.2

(CH_2), 35.2 (CH_2), 30.3 (CH_2), 29.6 (CH_2), 28.9 (CH_2), 28.8 (CH_2), 28.2 (CH_2), 28.0 (CH_2), 25.3 (CH_2), 22.6 (CH_2). HRMS (APCI) calculated for $C_{76}H_{109}N_6O_{20}S$ $[M+H]^+$ 1457.7412, found 1457.7428.

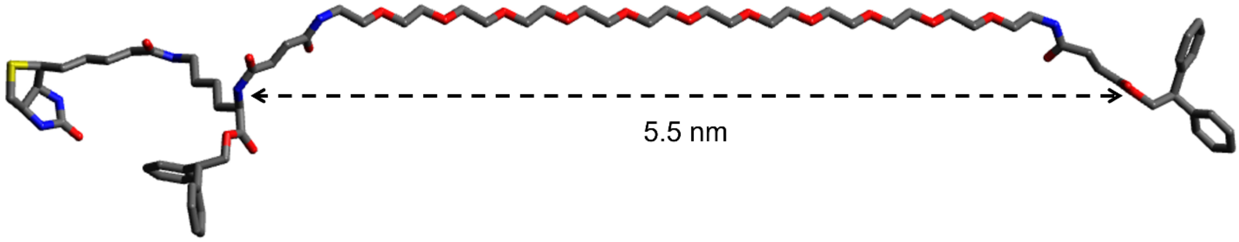

Figure S2: DFT calculations. The distance between the N terminal atom of the fumaramide station (green) and the O terminal atom of the succinic amide-ester station (orange) in thread **12** was 5.5 nm, as determined by DFT calculations. The polyethylene glycol spacer was commercially available as a mono-Boc-protected derivative (O-(2-Aminoethyl)-O′-[2-(Boc-amino)ethyl]decaethylene glycol), which facilitated the synthetic process compared to previous work of our laboratory.[S1] The Gaussian 09 program[S2] was used for geometry optimization. Energy minimization was performed at the density functional theory (DFT) B3LYP/6-31G(d,p) level of theory. The DFT optimized geometries were found to have zero imaginary frequencies.

Compound 13

5-aminoisophalic acid (2.5 g, 27.6 mmol) was dissolved in water (39 mL) at 0 ºC and 3 mL of 12 M HCl was added dropwise. $NaNO_2$ was then dissolved in water and added dropwise to the mixture, which was stirred for 30 min. Afterwards, NaN_3 was also dissolved in water and was added dropwise to the mixture. A yellow solid was formed, and gas evolution was observed. The mixture was stirred until gas evolution was no longer detected. The product was then filtered off, washed with distilled water, and dried under vacuum to get 5-azido-isophthalic acid (3.4 g, 60%). Next, oxalyl chloride (0.15 mL, 1.95 mmol) was added to a stirred suspension of 5-azido-isophthalic acid (100 mg, 0.48 mmol) and 2 drops of DMF in DCM (2 mL). The reaction mixture was stirred until the product was totally solubilized. The solvent was then removed under reduced pressure and the crude was kept under vacuum for 3 hours to remove the oxalyl chloride excess. The crude product was used directly in the next step without further purification. Its spectroscopic data were in concordance with those described in bibliography.[S1]

Compound 14

To a solution of *p*-xylylenediamine (515 mg, 3.78 mmol) in $CHCl_3$ (60 mL) at 0 ºC, a solution of Boc_2O (413 mg, 1.89 mmol) in $CHCl_3$ (45 mL) was added dropwise over a period of 4 hours. The mixture was stirred at room temperature overnight under an inert atmosphere. The resulting solid was filtered and washed with cold $CHCl_3$. Next, solvent was removed under reduced pressure, and DCM and water were added to the remaining oil. The layers were separated, and the aqueous layer was extracted with DCM. The organic phase was dried over anhydrous $MgSO_4$ and concentrated under reduced pressure. The crude was purified by column chromatography on silica gel using a gradient elution, from DCM/MeOH 95/5 to 85/15 to give *N*-Boc-4-(aminomethyl)benzylamine (400 mg, 90%). On the other hand, 2,6-pyridinedicarboxylic acid (234 mg, 1.4 mmol) and 2 drops of DMF were dissolved in dry DCM at 0 ºC, then oxalyl chloride was added dropwise. The reaction mixture was stirred until the product was totally solubilized. The solvent was then removed, and the crude solid was dried under high vacuum for 2 hours. The acid chloride formed was dissolved in $CHCl_3$ and added dropwise to a solution of the previously synthetized *N*-Boc-4-(aminomethyl)benzylamine, and Et_3N in $CHCl_3$. The reaction mixture was stirred overnight. Afterwards, the solvent was removed under reduced pressure and the remaining oil was dissolved in DCM and washed with water. The organic phase was dried over anhydrous $MgSO_4$ and concentrated under reduced pressure. The crude was purified by column chromatography on silica gel using a gradient elution, from DCM/MeOH 95/5 to 85/15 to give the Boc-protected precursor (400 mg, 90%). Finally, the Boc-protected precursor was dissolved in DCM at 0 ºC and TFA (0.30 mL, 4.00 mmol) was added dropwise at 0 ºC. The reaction was stirred at room temperature for 4 hours until it was completed (followed by TLC). Then, the solvent and excess of TFA were removed under reduced pressure and the crude was dissolved in a mixture DCM/MeOH 1/1 and Amberlyst® A21 was added. The mixture was stirred at room temperature for 1 hour. Afterwards, the resin was filtered, and the solvent was removed under reduced pressure, to furnish the unprotected amine **19**, which was used in the next step without further purification. Its spectroscopic data were in concordance with those described in bibliography.[S1]

Molecular shuttle 15

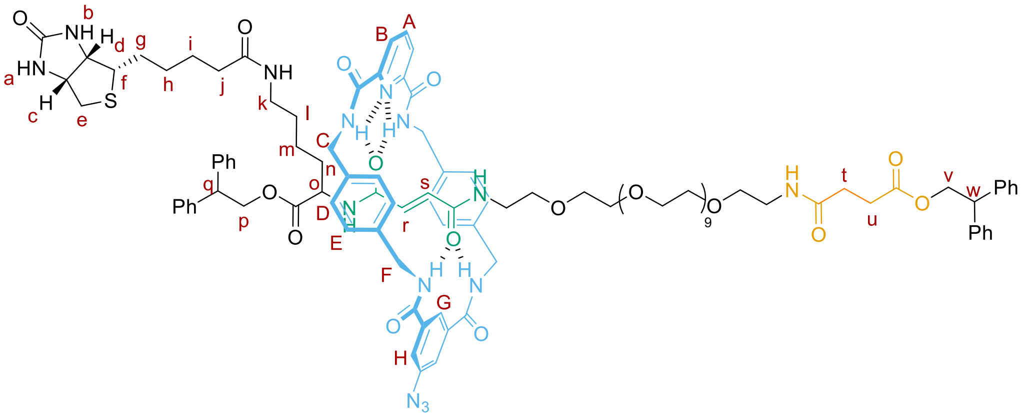

Thread **12** (30 mg, 0.02 mmol) and Et_3N (0.1 mL, 0.72 mmol) were dissolved in 4 mL $CHCl_3$ (stabilized with amylenes). The mixture was stirred vigorously whilst solutions of the diamine **14** (100 mg, 0.25 mmol) in $CHCl_3$ (3 mL) and the acid chloride **13** (61 mg, 0.25 mmol) in $CHCl_3$ (3 mL) were simultaneously added over a period of 3 hours using motor-driven syringe pumps. After 12 hours, the solvent was removed under reduced pressure and the resulting residue was purified by column chromatography on silica gel using a DCM/MeOH 92/8 mixture as eluent, to give the rotaxane **15** as colourless oil (15 mg, 46%). ^{1}H NMR (400 MHz, DMSO-d_6, 298 K) δ = 9.60 (m, 2H, NH), 8.74 (d, *J* = 6.8 Hz, 1H, NH), 8.53 (t, *J* = 5.6 Hz, 1H, NH), 8.34 (m, 1H, H_A), 8.23 (m, 2H, H_B), 7.91 (t, *J* = 4.6 Hz, 1H, NH), 7.84 (m, 2H, NH), 7.71 (t, *J* = 5.5 Hz, 1H, NH), 7.22 (m, 23H, H_{G+H+Ar}), 7.08 (m, 8H, H_{D+E}), 6.40 (br, 1H, H_a), 6.34 (br, 1H, H_b), 6.21 (m, 2H, H_{r+s}), 4.72 (dd, *J* = 10.9, 8.5 Hz, 1H, H_p or $H_{p'}$), 4.54 (m, 7H, $H_{p'}$ or H_p, H_v and H_C or H_F), 4.45 – 4.22 (m, 7H, H_c, H_q, H_w and H_C or H_F), 4.11 (m, 2H, H_d, H_o), 3.50 (m, 2H, PEG-H), 3.40 (m, 12H, PEG-H), 3.30 (m, 28H, PEG-H), 3.20 (m, 2H, PEG-H), 3.09 (m, 5H, PEG-H and H_f), 2.93 (m, 2H, H_k), 2.80 (dd, *J* =12.4, 5.1 Hz, 1H, H_e or $H_{e'}$), 2.57 (d, J = 12.4 Hz, 1H, $H_{e'}$ or H_e), 2.28 (t, *J* = 7.0 Hz, 2H, H_u), 2.16 (t, *J* = 7.0 Hz, 2H, H_t), 2.04 (t, *J* = 7.4 Hz, 2H, H_j), 1.48 (m, 12H, $H_{g+h+i+l+m+n}$). HRMS (ESI) calculated for $C_{107}H_{134}N_{14}O_{24}SNa$ $[M+Na]^+$ 2053.9308, found 2053.9285.

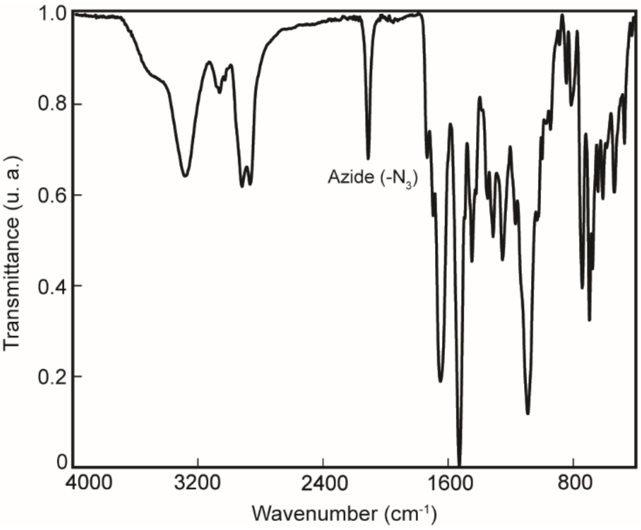

Figure S3: ATR-FTIR of molecular shuttle 15. Band from azide group ($-N_3$) appears at 2115 cm^{-1}.

A ^{1}H NMR spectrum comparison between the thread **12** (**Figure S4a**) and the molecular shuttle **15** (**Figure S4b**) was performed to corroborate its interlocked nature.

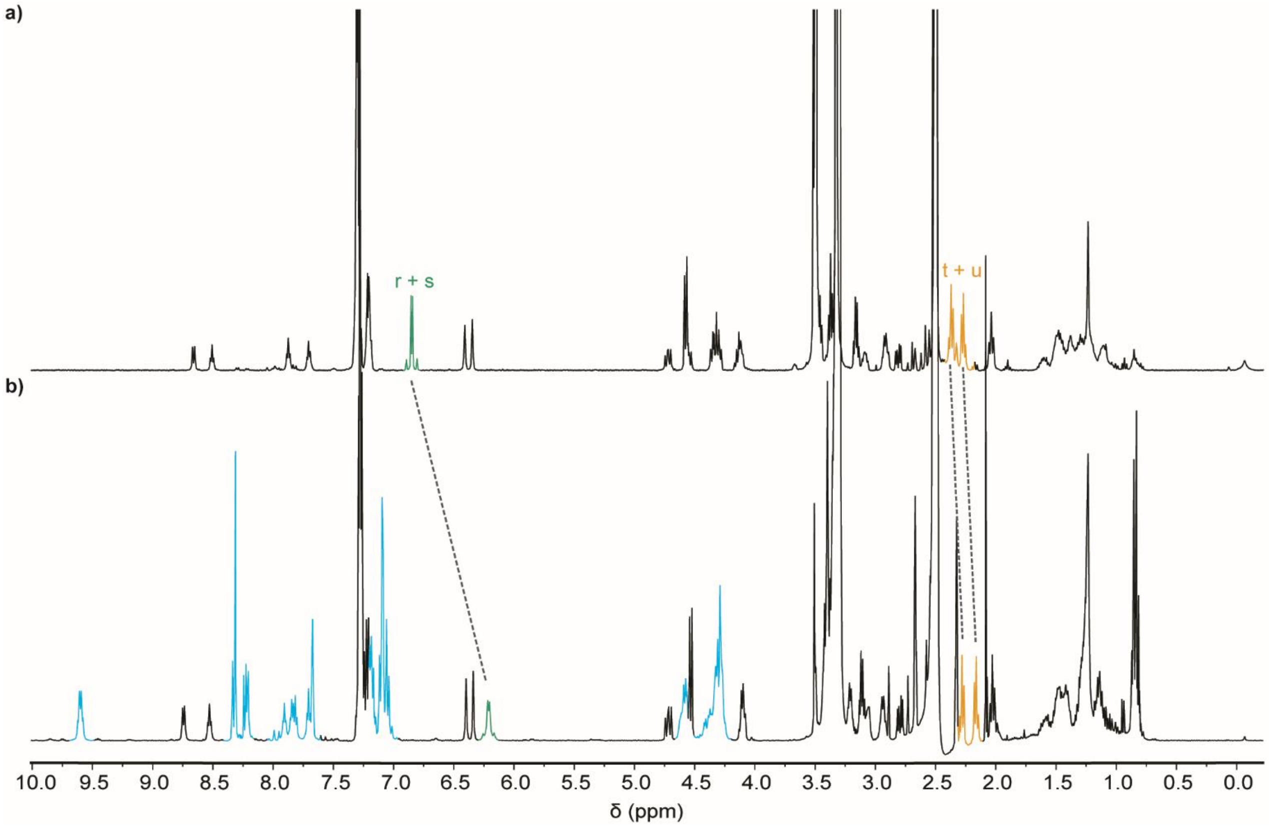

Figure S4. **^{1}H NMR spectra** (400 MHz, DMSO-d_6, 298 K): **a)** thread **12**; **b)** molecular shuttle **15**. The molecular shift displacement of fumaramide signals (*fum*, in green) and succinic amide-ester signals (*succ*, in orange) is due to the different diamagnetic shielding effect of the macrocycle over both stations. The higher displacement in the *fum* signals means the macrocycle (in blue) spends more time over it under these experimental conditions.

Molecular shuttle-dsDNA hybrid 19.

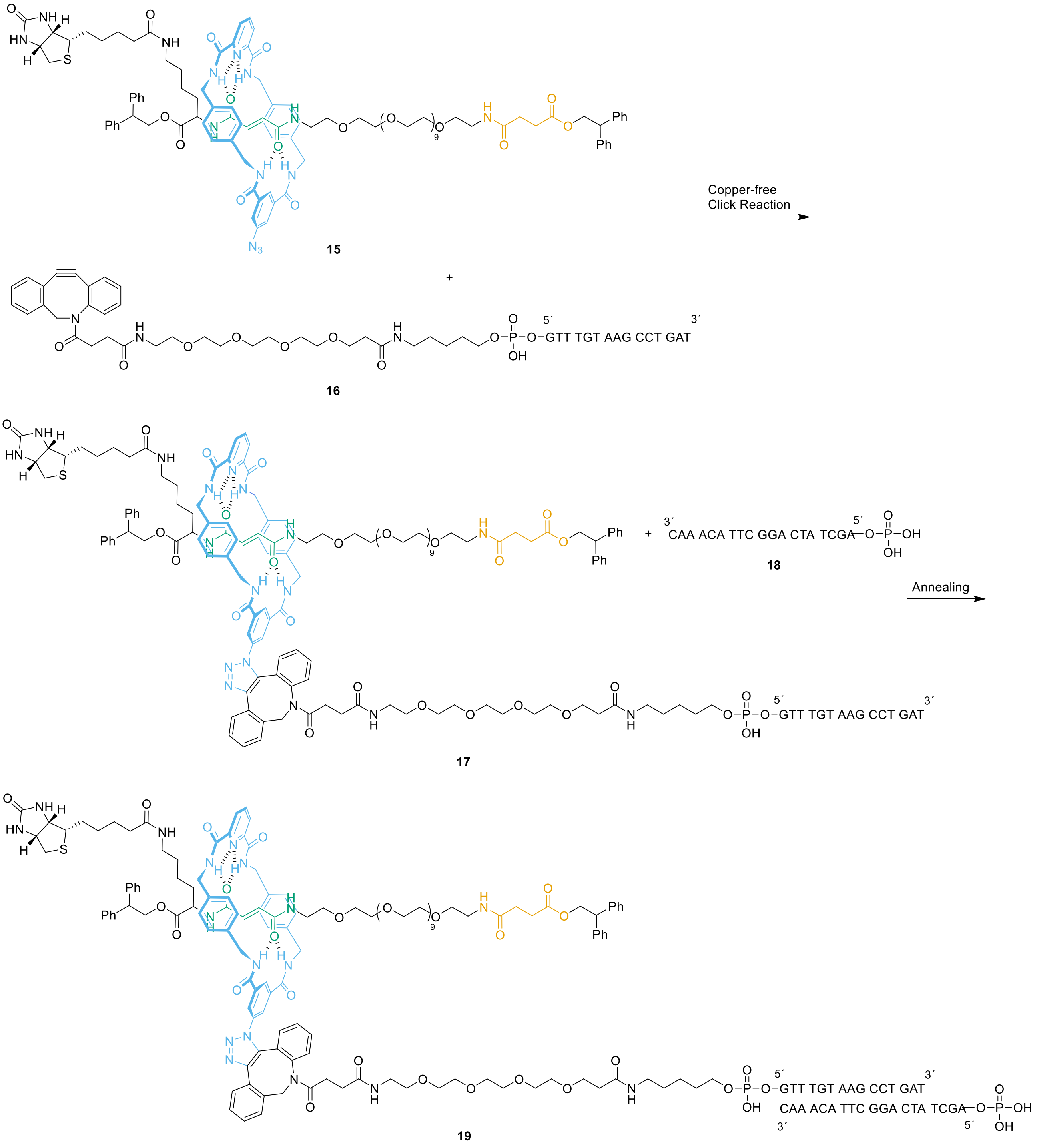

Figure S5. Preparation of the molecular shuttle-dsDNA hybrid **19**.

100 µM solutions of molecular shuttle **15** in DMF (75 µL) and ssDNA **16** (DBCO-PEG4-GTTTGTAAGCCTGAT) in water (35 µL) were mixed and 100 µL of Milli-Q® water was added to a final volume of 210 µL. The mixture was stirred at room temperature overnight. Afterwards, the solvent was eliminated in a SpeedVac™ vacuum concentrator and the molecular shuttle-ssDNA hybrid **17** was subsequently resuspended in 70 µL of Milli-Q® water. Next, 50 µM aqueous solutions of molecular

shuttle-ssDNA hybrid **17** (2 µL) and 100 µM oligonucleotide **18** (Phos-AGCTATCAGGCTTACAAAC) (1 µL) were mixed in 40 µL final volume of annealing buffer (20 mM Tris-HCl, 100 mM NaCl, 2 mM EDTA). The final mixture was incubated at 95 ºC for 5 minutes and then it was allowed to cool to 25 ºC gradually. In this way, the molecular shuttle-dsDNA hybrid **19** which contains the molecular shuttle at its end was prepared. In the opposite end, the annealed dsDNA holds a protruding AGCT 5' end, compatible with the 5' protruding end produced in a HindIII digestion.

3. NMR spectra.

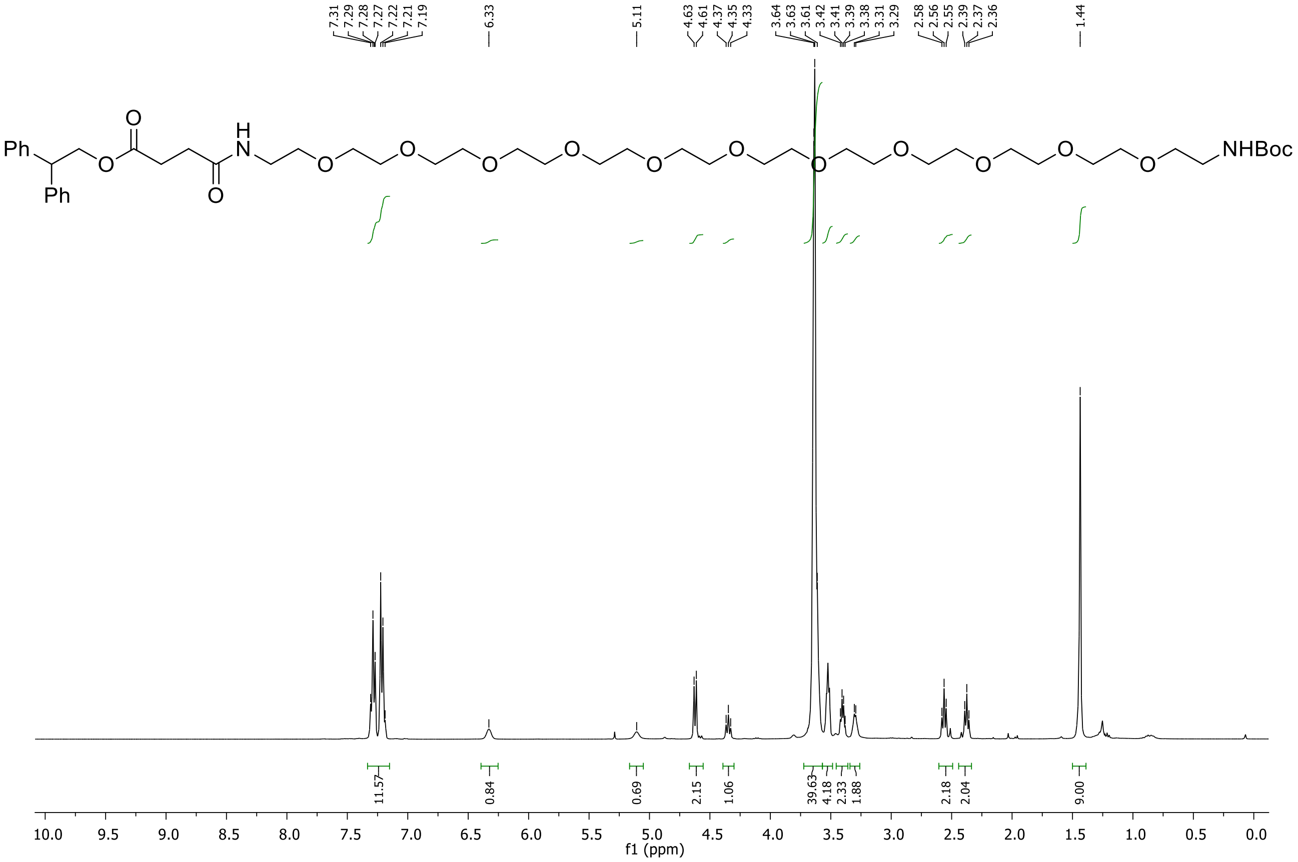

Figure S6: ^{1}H NMR spectrum of compound 9 (400 MHz, $CDCl_3$, 298 K).

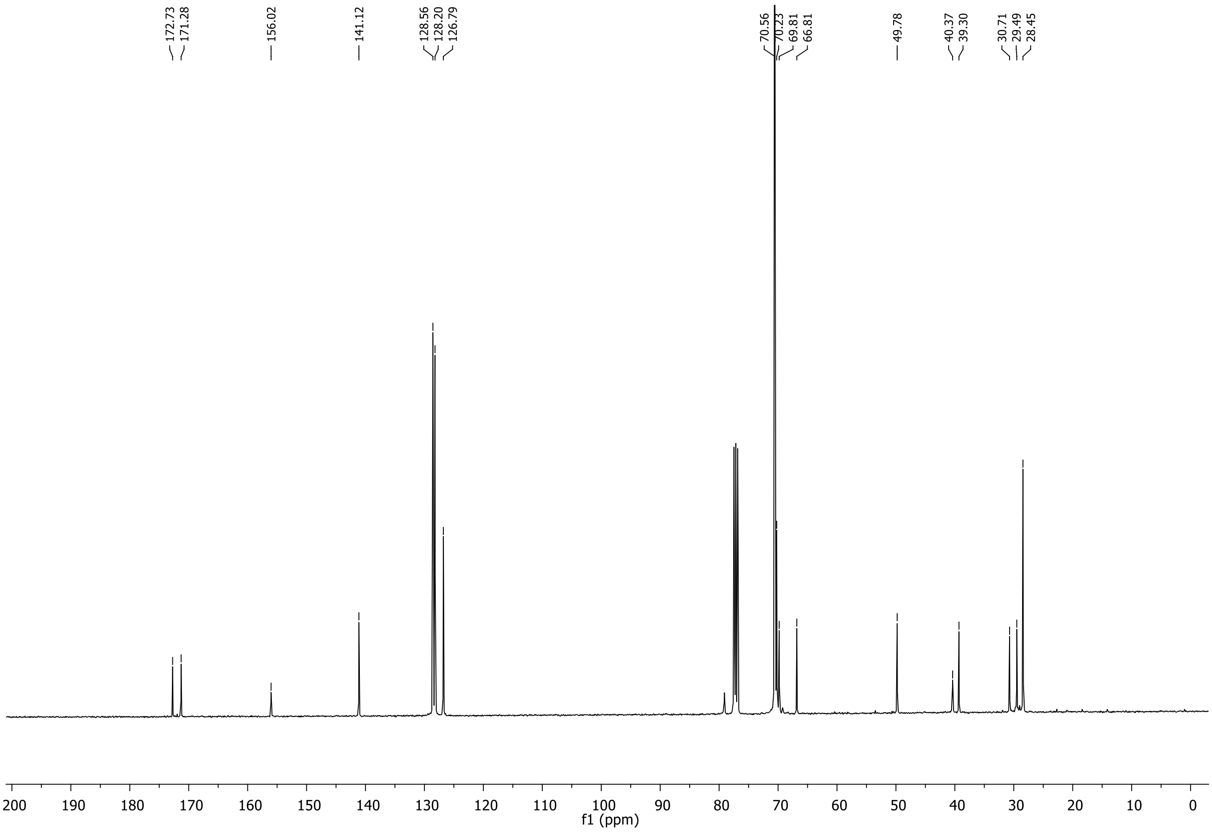

Figure S7: ^{13}C NMR spectrum of compound 9 (100 MHz, CDCl$_3$, 298 K).

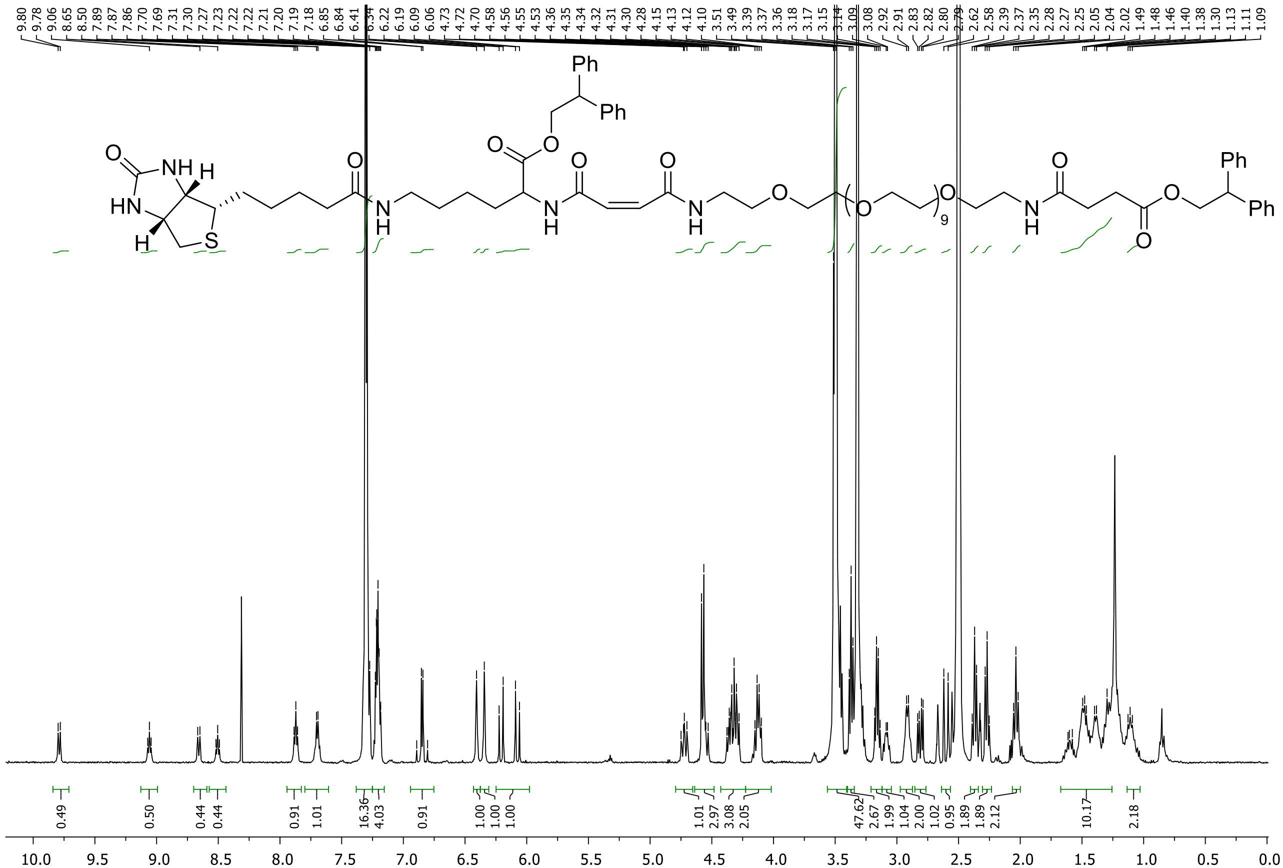

Figure S8: ^{1}H NMR spectrum of compound 11 (400 MHz, DMSO-d_6, 298 K).

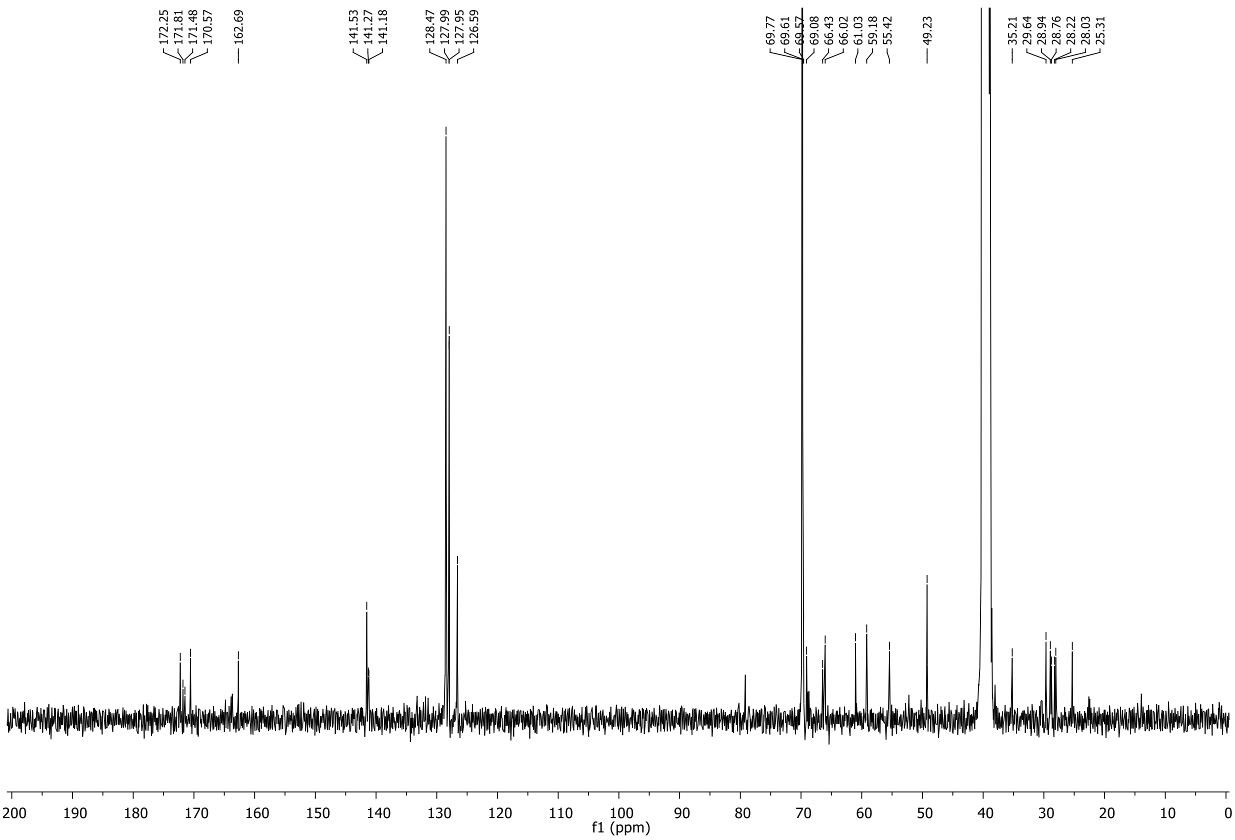

Figure S9: ^{13}C NMR spectrum of compound 11 (100 MHz, DMSO-d_6, 298 K).

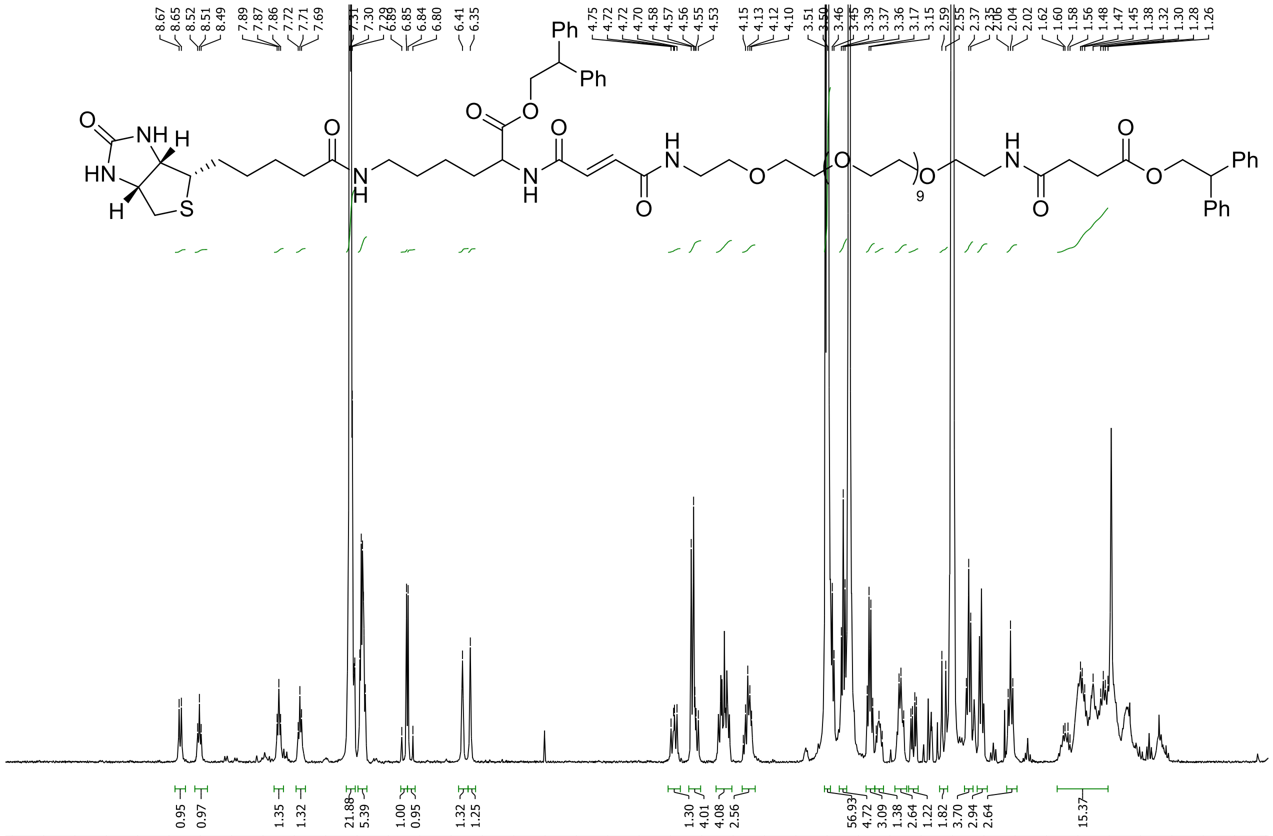

Figure S10: ^{1}H NMR spectrum of compound 12 (400 MHz, DMSO-d_6, 298 K).

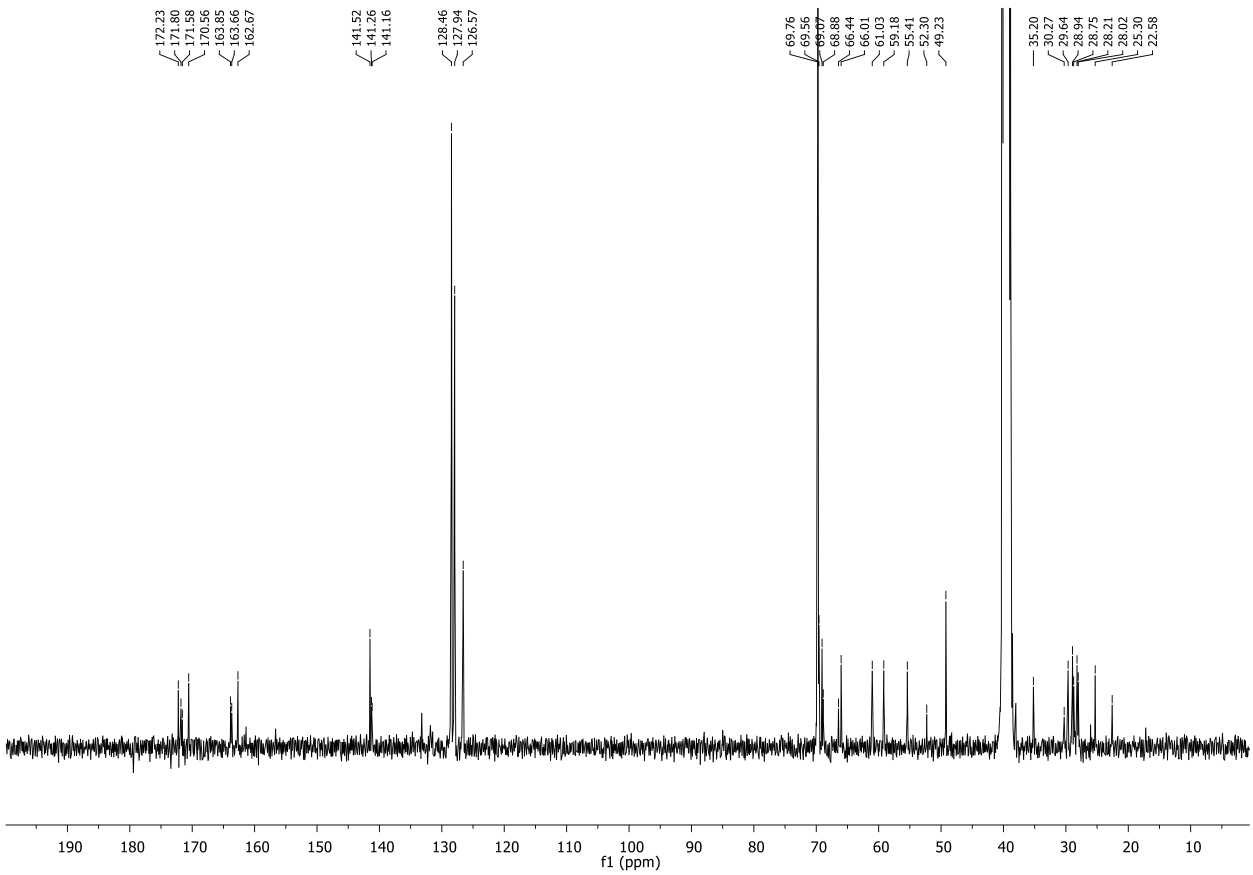

Figure S11: ^{13}C NMR spectrum of compound 12 (100 MHz, DMSO-d_6, 298 K).

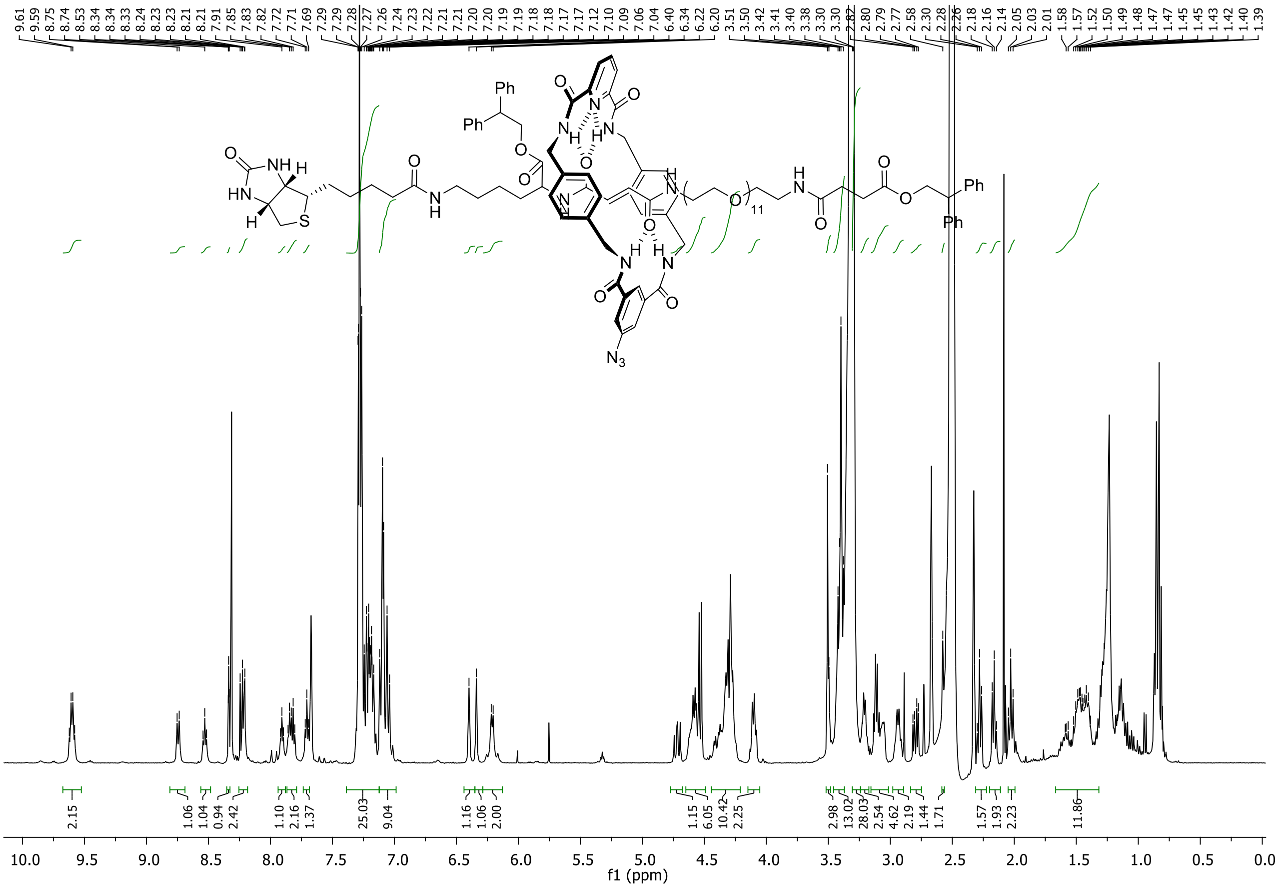

Figure S12: ^{1}H NMR spectrum of compound 15 (400 MHz, DMSO-d_6, 298 K).

4. High Resolution Mass Spectrometry.

In each figure, the upper spectrum corresponds to the experimental isotopic distribution and the lower one corresponds to the theoretical isotopic distribution.

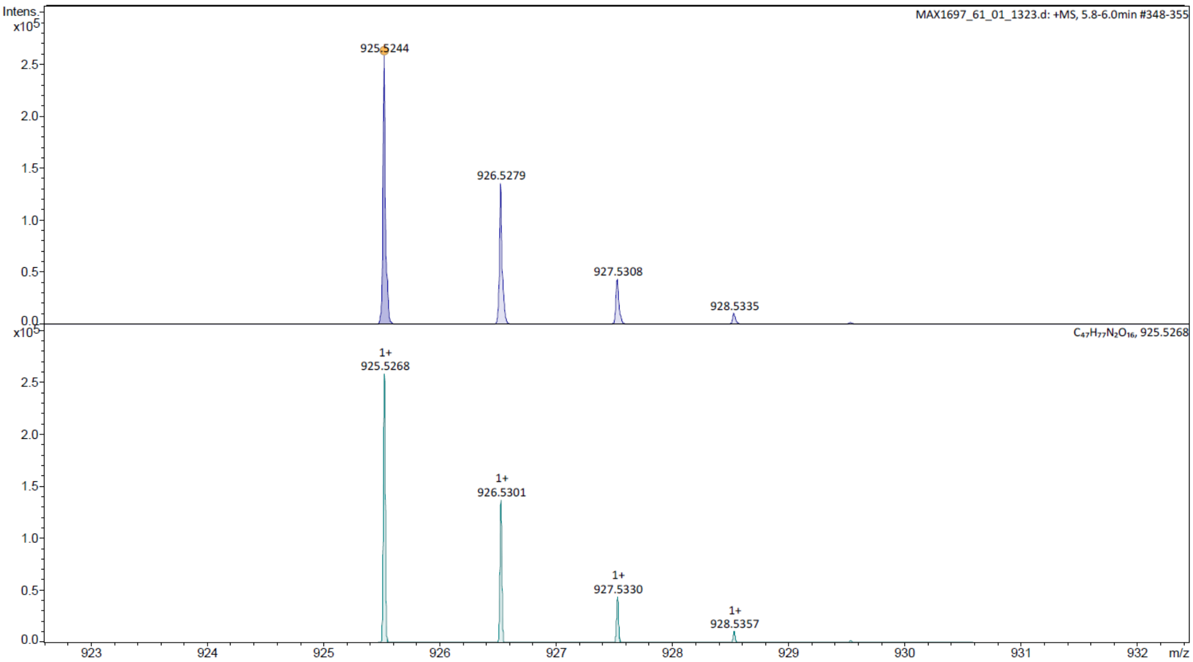

Figure S13: HRMS (APCI) spectra of compound **9**.

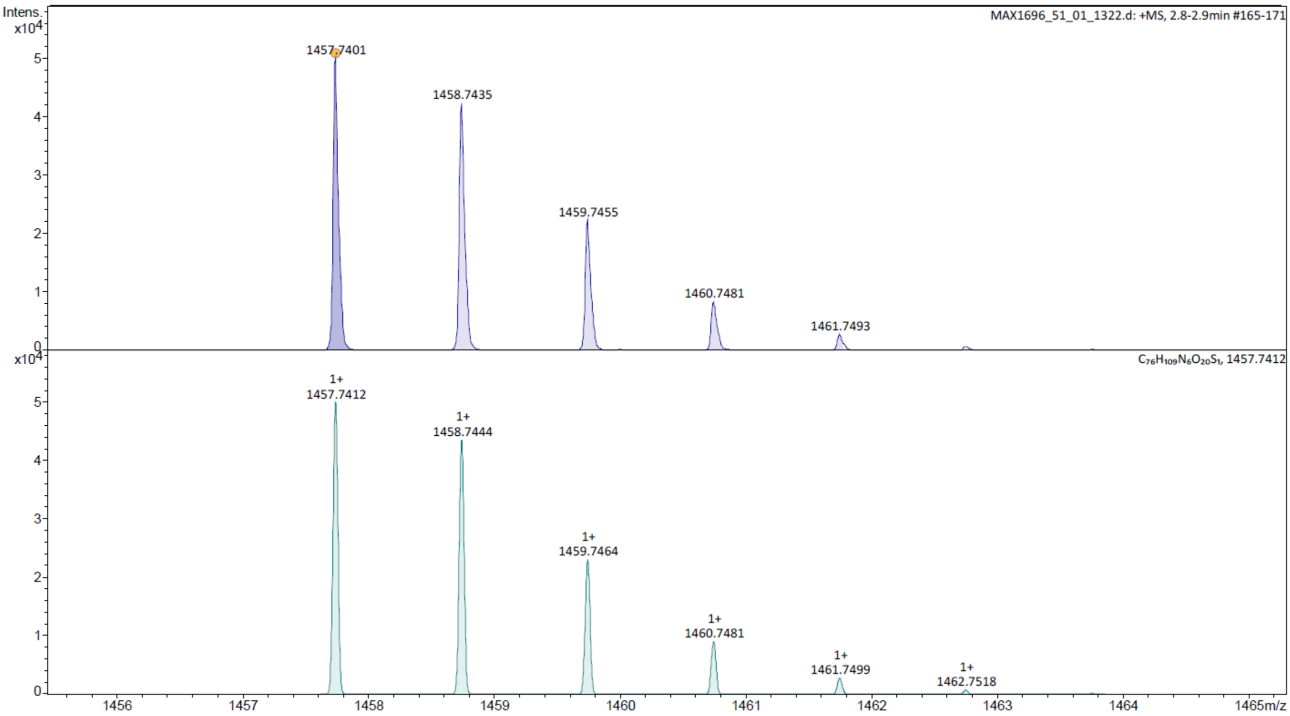

Figure S14: HRMS (APCI) spectra of compound **11**.

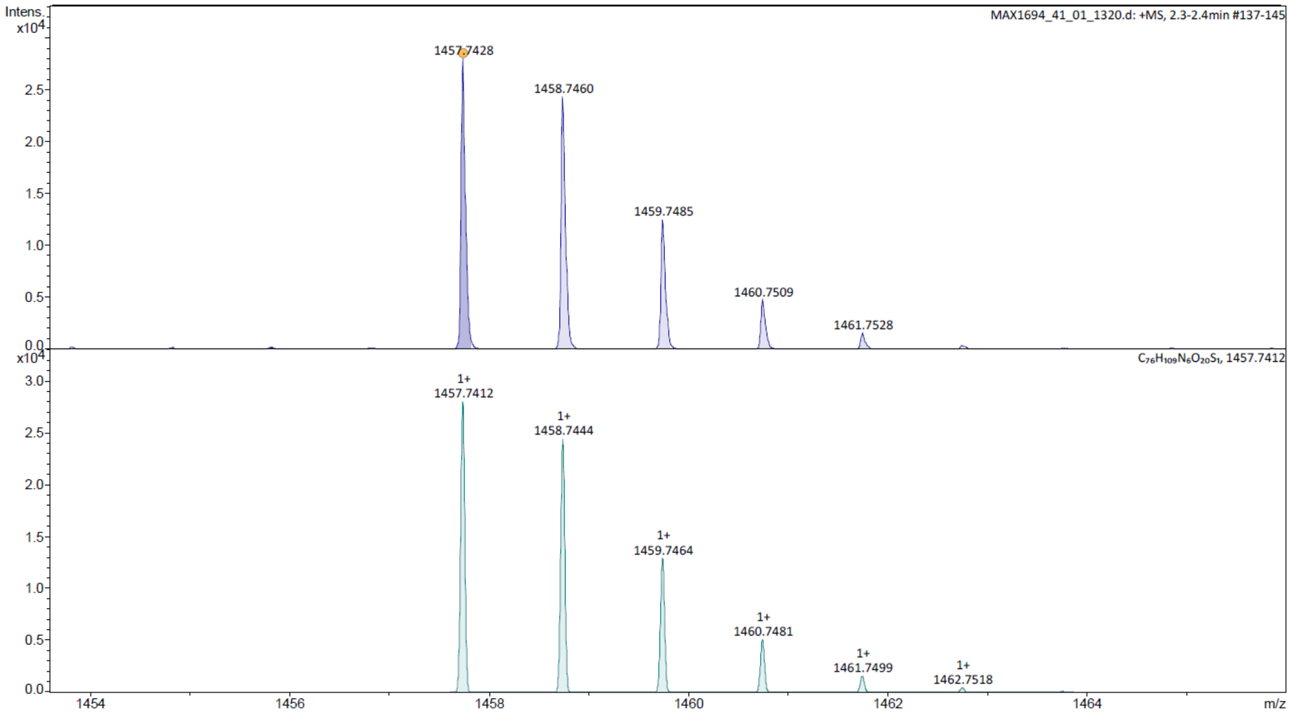

Figure S15: HRMS (APCI) spectra of compound 12.

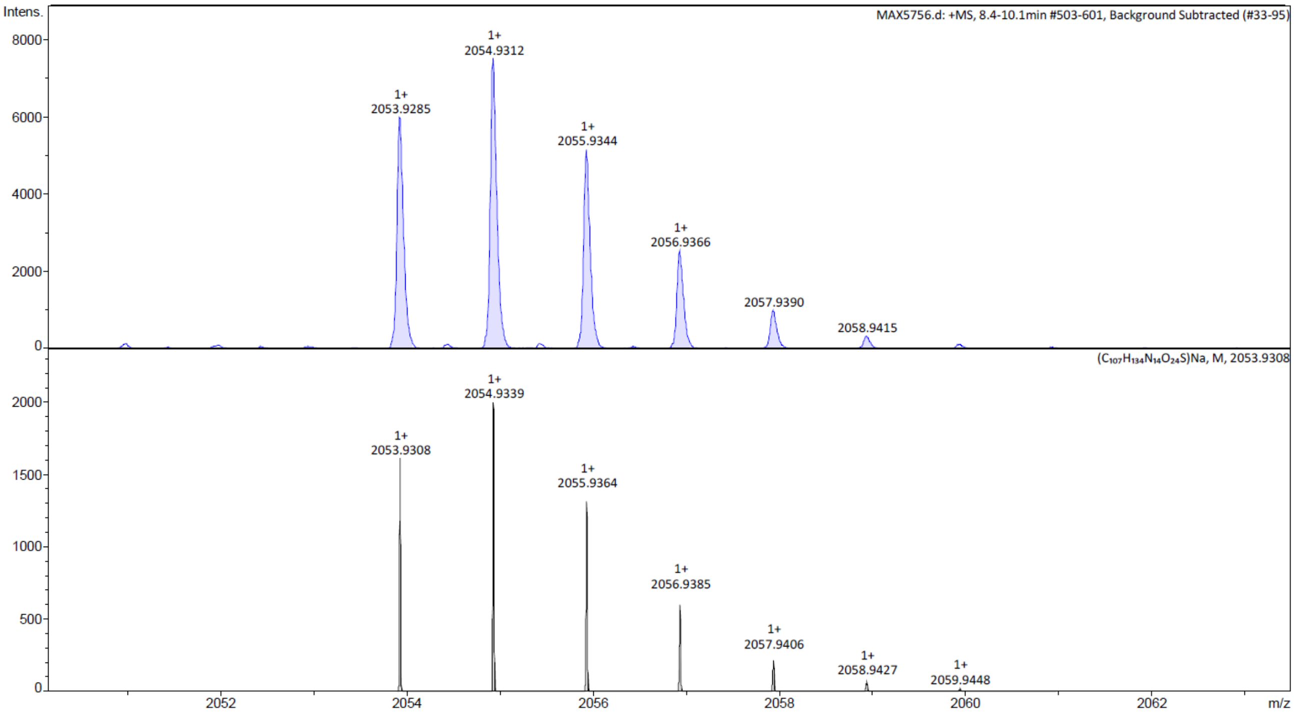

Figure S16: HRMS (ESI) spectra of compound 15.

5. Coupling of the molecular shuttle-dsDNA hybrid 19 to DNA handles.

The molecular shuttle was connected between two functionalized beads using two dsDNA handles for optical tweezers experiments. The shorter 837 bp dsDNA handle that will connect the thread of the molecular shuttle to the micropipette-bead via streptavidin-biotin attachment was synthetized by PCR amplification of a section of the pUC19 vector with two DNA oligonucleotides: one labeled with biotin and the other with digoxigenin at the 5′-end. The handle was then incubated with saturating amounts of streptavidin and attached to anti-digoxigenin covered polystyrene micron-beads (Spherotech, Co). One of these beads is held by suction on top of a micropipette in the microfluidic chamber.

On the other hand, a longer 2701 bp dsDNA handle connects the macrocycle to the bead in the optical trap. This handle was obtained from the pUC19 vector (Novagen) using restriction digestion with BamHI and HindIII endonucleases. In a single step, the digestion result was ligated at the BamHI end with a DNA segment labelled with numerous digoxigenin units,[S3] and at the HindIII end with molecular shuttle-dsDNA hybrid **19**, which has 15 additional base pairs.

The final molecular shuttle-dsDNA hybrid was then linked to anti-digoxigenin-coated beads (Spherotech Co.) and these diluted in the measurement buffer before being flowed into the fluidic chamber, where they can be manipulated using the optical trap. Individual molecular shuttle-dsDNA hybrids must be tethered after attaching the molecular shuttle's biotin end to the streptavidin unit at the extreme of the 837 bp dsDNA handle, which is in turn linked to the micropipette-bead.

6. General considerations on optical tweezers experiments and analysis.

Optical tweezers measurements were performed at 22 ± 1 °C with a highly stable miniaturized dual-beam optical tweezers,[S4] with a limiting spatial resolution of ≤ 1 nm.

Pulling-relaxing cycles were recorded at a constant pulling rate of 200 nm s^{-1}. The setup controls the distance between the trap center and the micropipette tip (X_{total}) which differs from the end-to-end distance of the tethered molecular system under consideration ($X_{end-end}$). The system's end-to-end distance is computed by the following formula:

$$X_{end-end} = X_{total} - \frac{F}{k} \quad \textbf{(equation S1)}$$

where F is the force applied to the system, k the stiffness of the trap, and $\frac{F}{k}$ corresponds to the distance traversed (in nm) by the bead out of the trap center (bead position). We assume a linear spring restoring force. The stiffness of the trap depends on the power of the lasers, the size and refractive index of the bead in the trap as well as the viscosity of the surrounding medium. In our experimental conditions, for the 3 μm diameter beads employed and a laser power of 60 mW, the value of the stiffness is k = 0.135 ± 0.004 pN/nm. A feedback stabilized protocol was used for constant force measurements, that maintain them within ~0.05 pN by moving the beads closer or further apart. All experimental data was recorded at 0.5 kHz.

In this study, 8 individual molecular shuttles were analyzed. To conduct this, the optically trapped bead, decorated with the molecular shuttle, was positioned close to another bead held by a micropipette to facilitate a specific biotin-streptavidin interaction. This interaction tethered the molecular shuttle-dsDNA hybrid end-to-end in the experimental setup. Each molecular system was subjected to pulling- relaxing cycles. The resulting force-extension curves fitted well with a worm-like chain model (WLC) of a polymer, showing a persistence length of 50 nm, consistent with known values for dsDNA chains, thus confirming the single-molecule conditions (see **section 7**).

Once single-molecule conditions were confirmed, we conducted hopping experiments using a force-feedback protocol, applying various constant forces until the end-to-end attachments were disrupted. Working at this molecular scale is challenging, as the system could fail due to environmental mechanical disturbances or excessive forces that compromised anchoring points. From the total hopping traces obtained, 12 were selected for this study, each long enough to analyze, with forces ranging from 9 to 9.9 pN. Due to the statistical nature of the LTFT analysis, shorter traces (less than 15 seconds) were excluded to ensure sufficient event transitions for meaningful statistical distributions. The raw hopping traces were baseline-corrected by fitting a polynomial function (of order 1 to 3, depending on the trace). Unstable traces that did not fit well to a polynomial were also discarded from this analysis. The baseline correction algorithm, developed in Matlab, is available at https://hdl.handle.net/20.500.12614/3812.

7. Pulling-relaxing cycles.

Figure S17a displays a representative pulling-relaxing cycle (force-extension curve) taken in aqueous conditions at 20 mM Tris-HCl 150 mM NaCl by retraction of the optical trap at a constant velocity of 200 nm s^{-1} at 22 ± 1 ºC. The black curve corresponds to the pulling cycle and the blue curve corresponds to the relaxing cycle. Individual molecular shuttle-dsDNA hybrid attachments must have a response in force-extension curves that fits to a worm-like chain model (WLC, **equation S2**) describing the elastic properties of the dsDNA handles:

$$x = L_c \cdot \left[1 - \frac{1}{2} \cdot \sqrt{\frac{K_B T}{F \cdot L_p}} + \frac{F}{S}\right] \qquad \textbf{(equation S2)}$$

where x and F are the extension and force; $L_c = 0.34 \cdot bp$ is the contour length (being bp the number of base pairs), L_p the persistence length, S the stretching modulus, and $K_B T = 4.114\, pN \cdot nm = 0.14\, \frac{kcal}{mol}$.[S5]

Green and orange lines in **Figure S17a** are fittings to the WLC before shuttling from *fum* to *succ* and after shuttling from *succ* to *fum* station, respectively. At low pulling forces the force-extension curves fit well to a WLC of a polymer with $L_p = 50\, nm$ and $S = 1100\, pN$, characteristic of a single dsDNA molecule (green curve, **equation S2**).[S6] After the shuttling, the experimental data have been adjusted to a modified model considering a WLC response (**equation S2** for the dsDNA handles) plus a constant Δx accounting for the displacement of the curve due to the shuttling of the macrocycle between stations within the molecular shuttle. The obtained value of Δx is 15.1 ± 0.1 nm (N = 59).

The mechanical strength of the H-bonding interaction between macrocycle and stations as well as the coexistence force were determined from the histogram in **Figure S17b**, constructed with all the breaking forces gathered from 59 pulling-relaxing cycles of individual molecular shuttle-dsDNA hybrids. In **Figure S17b**, the gaussian distributions fitted to the breaking force histograms yield the rupture forces at each station (F_{succ} in orange and F_{fum} in green). The coexistence force ($F_{1/2}$), calculated as the intersection point of both gaussian distributions (gray dashed line), is 9.4 ± 0.8 pN. The value of the calculated coexistence force is consistent with that of a similar molecular shuttle determined by us previously under similar experimental conditions.[S1] Note that due to the stochastic nature of single molecule experiments, F_{succ} and F_{fum} are not constant values and exist as a probability distribution, i.e., different individual molecular shuttles show breaking forces at similar yet different values. Hence, the $F_{1/2}$ calculated is a statistical parameter that represents an average value for all the molecules probed. Individually, a single molecular shuttle can show coexistence at higher or lower values. The value of $F_{1/2}$ retrieved from pulling-relaxing experiments explained above matches the value obtained applying Bell-Evans theory to the hopping traces as detailed below (**section 11**).

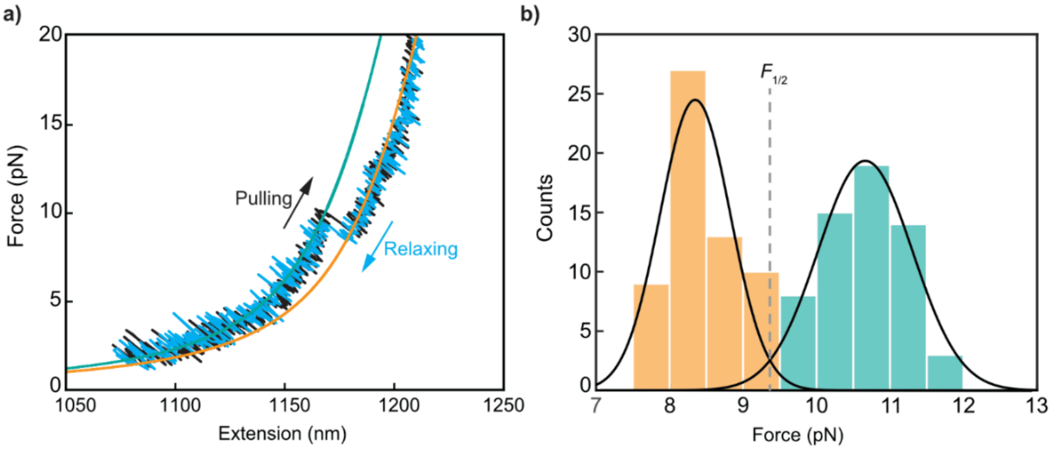

Figure S17: Pulling-relaxing cycles. **a)** Representative pulling-relaxing cycle of an individual molecular shuttle. Pulling curve is represented in black and relaxing curve in blue. Fitting to the WLC model is displayed by green and orange lines before shuttling from *fum* to *succ* and after shuttling from *succ* to *fum* station, respectively. **b)** Determination of breaking forces at each station. Orange (*succ*) and green (*fum*) histogram represent the breaking rupture forces gathered for each station in pulling-relaxing cycles of individual molecules at a pulling rate of 200 nm s^{-1} (N = 59). Each histogram fits to a gaussian distribution yielding: F_{succ} = 8.3 ± 0.7 pN and F_{fum} = 10.7 ± 0.8 pN. The intersection between the two gaussian fits (grey dashed line) yields the coexistence force, $F_{1/2}$ = 9.4 ± 0.7 pN.

8. Effect of DNA handles length on hopping experiments.

The experimental shuttling distance recovered from hopping traces in the main text is 15.2 ± 0.8 nm, far from the theoretical maximum distance of 5.5 nm, calculated by DFT. **Figure S18** displays hopping traces of the molecular shuttle-dsDNA hybrid using both 3538 bp (2701 upper + 837 lower) handles and 120 bp (60 bp upper + 60 bp lower) handles. The distance recovered between stations is 15.2 ± 0.8 nm, and 5.3 ± 0.8 nm for long and short handles, respectively. Therefore, the length of the DNA handles used affects the measured extension, and shorter handles allow us to recover the theoretical values expected for distance between stations. The reason behind this effect is currently under investigation in our lab and might be related with a DNA stretching upon shuttling that contributes to the total measured distance.

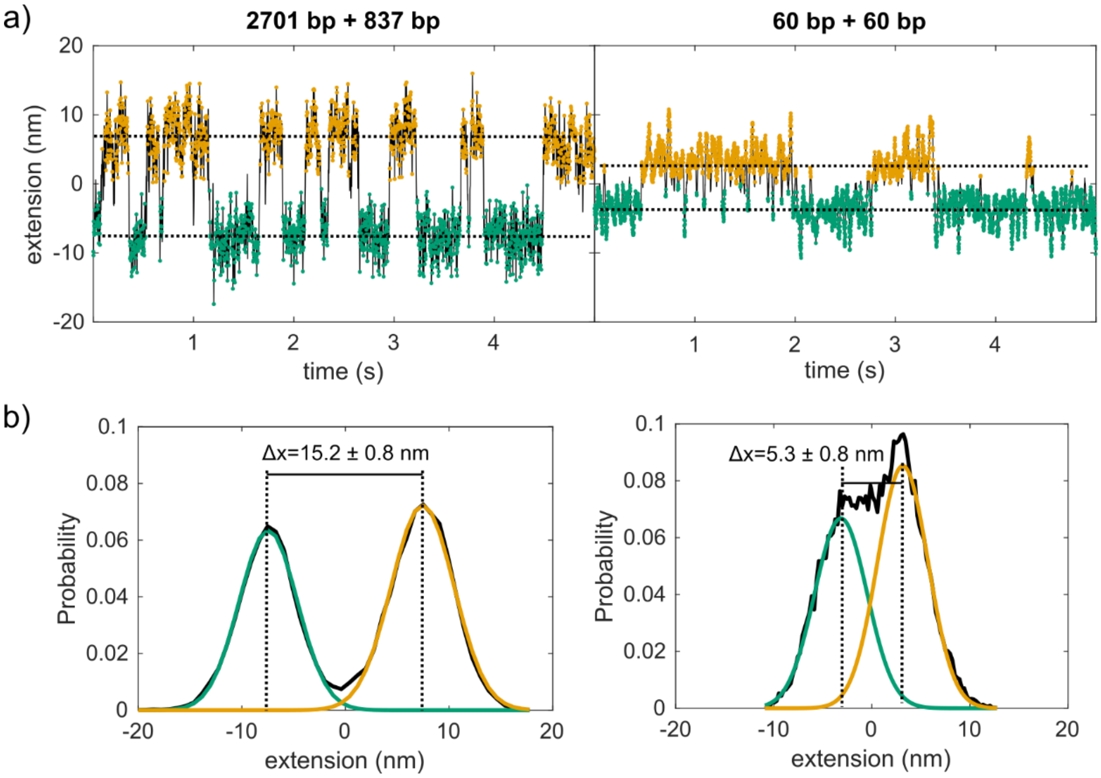

Figure S18: Effect of DNA handles length on experimental distance. **a)** Extension *vs* time traces of a molecular shuttle-dsDNA hybrid using a total number of base pairs in both handles of 3538 (left, 2701 bp top handle and 837 bp bottom handle) and 120 (right, 60 bp top handle and 60 bp bottom handle). Dashed lines indicate the center of the gaussian probability distributions at the *fum* (green) and *succ* (orange) stations. **b)** Normalized probability distributions of the traces in a. Black line corresponds to the experimental data and green and orange lines to gaussian fits for *fum* and *succ*, respectively. The distance between the gaussian distributions is 15.2 ± 0.8 and 5.3 ± 0.8 nm for long and short handles, respectively.

In **Figure S19** we include the calculation of τ_{tp} as defined in the main text for long (**a** and **b**) and short handles (**c** and **d**). See **section 9** for details on the calculation. The symmetry of τ_{tp} in opposite directions is proven in both cases which confirms the LTFT principle, independently of the total distance change between stations. Experimentally, working with short handles is challenging due to the small distance between beads that reduces drastically the success rate of tethering an individual shuttle. In this study we continued using the longer handles (2701 + 837 bp for top and bottom handle, respectively) for the shake of simplicity and to improve statistics and significance of our results, given that it does not affect the transition times calculations relevant in this work.

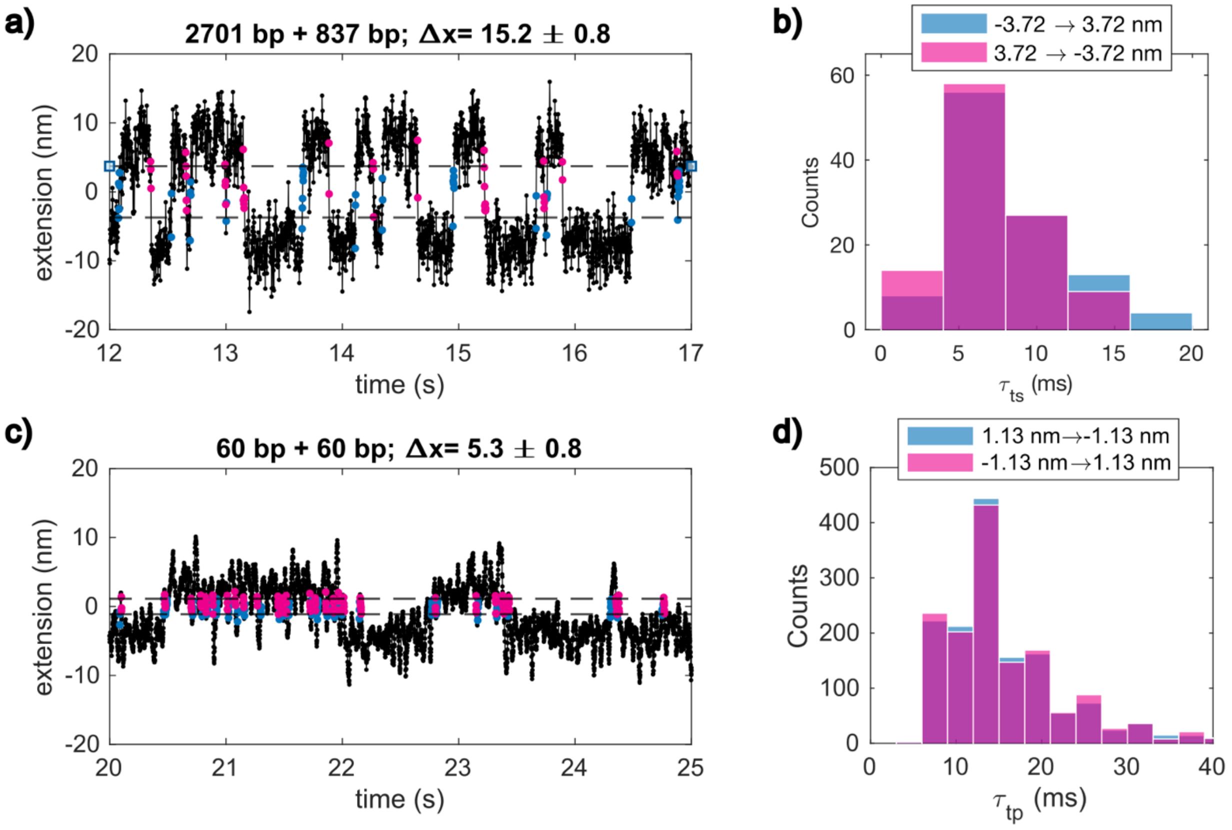

Figure S19: Effect of DNA handles length on $\boldsymbol{\tau_{tp}}$. Extension *vs* time traces of a molecular shuttle-dsDNA hybrid with a total number of base pairs in both handles of **a)** 3538 (2701 bp top handle and 837 bp bottom handle) and **c)** 120 (60 bp top handle and 60 bp bottom handle). Pink and blue dots indicate the datapoints within transition events from *succ* to *fum*, and *fum* to *succ* stations, respectively. The spatial limits for τ_{tp} are chosen as half of the mean position of *fum* and *succ* stations (exact values indicated in legend). The corresponding distribution of τ_{tp} are represented in **b)** hopping trace at coexistence (equivalent to **Figure 2**) and **d)** 5 hopping traces analyzed at coexistence for long and short dsDNA handles, **a)** and **c)**, respectively.

9. Calculation of transition times and quantification distribution symmetry.

The calculation of transit time (or LTFT) depicted in **Figures 2-3** in the main text (also **Figures S19, S22 and S123** in this document) requires only the definition of starting and final points *a* and *b* (or boundaries) describing the trajectory of the macrocycle within the axel to be analyzed. For a given hopping trace (extension *vs* time traces at constant force), we check the number of data points (or time) that it takes to go from *a* to *b* and from *b* to *a* (blue and pink dots, respectively, in **Figures 2-3** in the main text). This is automatically done through a Matlab algorithm that first identifies the datapoints at which the trace crosses the defined boundaries, and then computes the successful transitions in both directions *a*→*b* and *b*→*a*. A transition is considered successful only when there is a direct displacement between *a* and *b* (or *b* and *a*), i.e. after crossing the starting point, *a*, the trace goes to *b* without returning to *a* (*vice versa* for *b*→*a*). After computing all the existing transitions, *a*→*b* and *b*→*a*, the distributions are plotted as histograms that show symmetry (as discussed in main text and further explored in **section 10** and **12**), with almost identical values for mean and median.

To test the equality between distributions (and identify any possible variance) we independently performed a two-sample Kolmogorov-Smirnov test (K-S) and a Mann-Whitney U-test (M-W) for each set of transition times calculated.[S7-S9] These non-parametric tests are designed to find statistically significant differences between population distributions and we include a power estimation that considers the actual number of transitions measured experimentally, their mean and standard deviations, an effect size of 0.5 times the standard deviation and a significance level of 95%. The power estimates the likelihood that the test will detect a true difference between distributions if it exists, and we consider power values above 80% in either of the tests performed, sufficient to claim symmetry. We use the build-in functions in Matlab '`kstest2`' and '`ranksum`', for the K-S and M-W tests, respectively, and a simulation for the calculation of powers. The analysis procedure, including the calculation of transition times and significance tests are freely available at https://hdl.handle.net/20.500.12614/3812.

10. Significance test for transit times distributions (τ_{tp}).

The distributions of τ_{tp} presented in **Figure 2** of main text are symmetric for opposite paths (*a* → *b* and *b* → *a*) in all cases. **Table S1** summarizes the main statistical parameters where mean and median values are equal within error. Additionally, K-S and M-W Tests confirm the symmetry of the distributions, with p-values above 0.03 in all cases (a p-value below 0.03 sets the limit at which the test detect significant differences between distributions) except for the M-W Test at 9.1 pN (first column in table). Since the K-S test confirms symmetry with 97% power and means and median are equal within error, we conclude that the failure of the M-W test in this case is not significant, or representative of an overall trend observed when all the traces are considered. Additionally, note that the power estimation for the trace at 9.5 pN does not reach the 80% limit in any of the test, due to the small number of events (*n*), that decrease the detection efficiency. Still, identical values of mean and medians support the claim of symmetry in this case.

Force (pN)		9.1	9.3	9.4	9.5	9.9
Boundaries (a⇄b, nm)		-3.68 ⇄ 3.68	-3.97 ⇄ 3.97	-4.14 ⇄ 4.14	-4 ⇄ 4	-3.9 ⇄ 3.9
$\tau_{ts}(a \rightarrow b)$	***n***	156	1075	108	53	66
	Mean (ms)	8.2	9.3	7.1	4.6	9.8
	Median (ms)	8	8	6	4	10
	St. Dev. (ms)	4.1	4.1	3.5	1.8	4.7
$\tau_{ts}(b \rightarrow a)$	***n***	155	1075	108	54	67
	Mean (ms)	7.4	9.1	6.3	4.6	8.5
	Median (ms)	6	8	6	4	8
	St. Dev. (ms)	4.5	4.1	3.2	3	4.5
K-S Test	***p-val***	0.2	0.55	0.72	0.75	0.63
	power	97%	100%	89%	60%	67%
M-W Test	***p-val***	0.028	0.22	0.85	0.19	0.09
	power	99%	100%	95%	70%	80%

Table S1. **Statistical parameters retrieved from the τ_{tp} distributions shown in Figure 2**. Boundaries *a* and *b* are defined as half the mean value of the position of *fum* and *succ* stations, respectively; n corresponds to the number of events (transitions) counted for each trajectory; *St. Dev.* Is the standard deviation. K-S and M-W stand for Kolmogorov-Smirnov and Mann-Whitney tests. Values in red indicate low detection efficiency (or power) or failure passing symmetry tests.

11. Constant force experiments (hopping experiments).

In constant force measurements (force feedback mode) we monitor thousands of individual shuttling events in real time. The population distribution at each station is well described by gaussian probability distributions where the shuttling dynamics of the macrocycle is inferred by measuring the change in molecular extension (**Figure S18**). To obtain the shuttling rates for *fum* and *succ* stations, we first calculate the residence times at each station for several forces. An example of this procedure is depicted in **Figure S20** for three different forces. According to the Bell-Evans theory for a bistable system under near-equilibrium conditions,[S10,S11] the histograms of residence times obtained for each station can be fitted to an exponential decay whose decay constant is the shuttling rate (k_{fum} and k_{succ}), which is the inverse of the residence time of the macrocycle at each station. The values for k for each station and trace are summarized in **Table S2**.

		$F < F_{1/2}$	$F \approx F_{1/2}$	$F > F_{1/2}$
k **(s^{-1})**	k_{succ}	13.9 ± 1.7	9 ± 1	2.9 ± 0.5
	k_{fum}	3.0 ± 0.6	5.3 ± 0.7	41 ± 10

Table S2. Summary of shuttling rates at 3 different constant forces.

From experiments performed at several forces close to the $F_{1/2}$, the obtained shuttling rates show an exponential dependence on force and fit well to the Bell-Evans model along the entire range of forces measured, confirming the shuttling occurs under near-equilibrium conditions. Therefore, by plotting the natural logarithm of the shuttling rates as a function of force, the intersection of the two linear fits renders $F_{1/2}$ ≈ 9.4 pN (**Figure S20d**), which fully agrees with that extracted from the pulling-relaxing cycles (9.4 ± 0.7 pN, **section 7**).

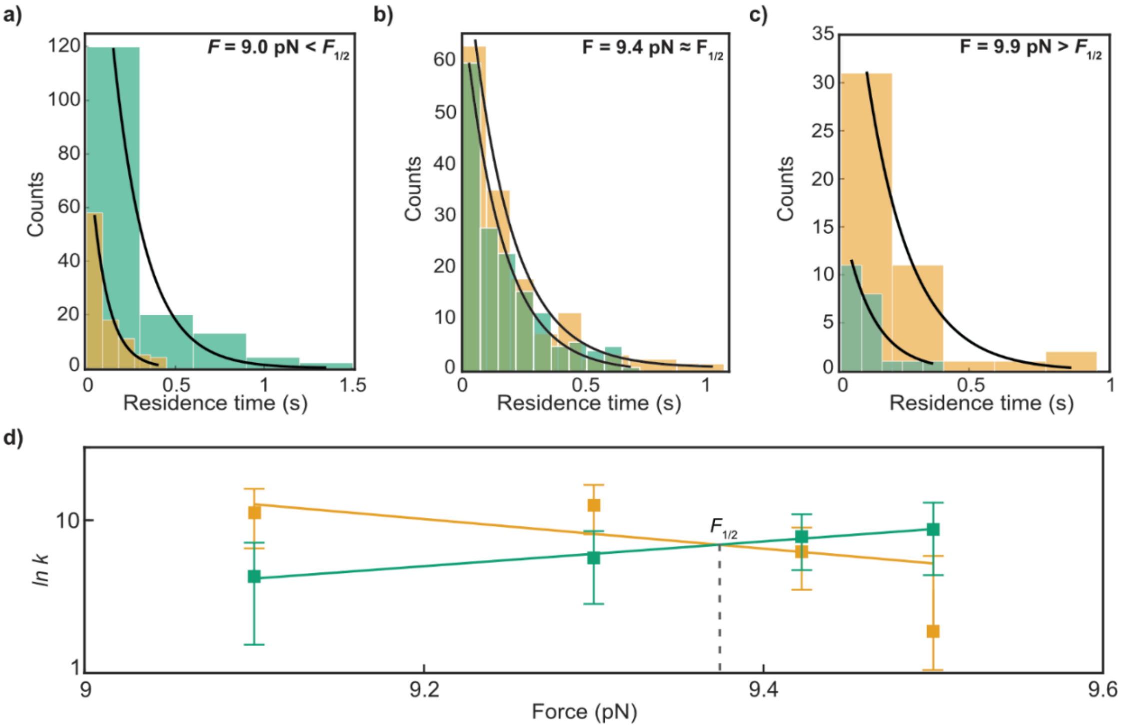

Figure S20: Examples of residence time distributions at different constant forces. Green (orange) histograms represent the values for the macrocycle at the *fum (succ)* station and black lines fit the exponential behavior of the residence time at each station: **a)** F = 9.0 pN < $F_{1/2}$, as expected for forces below coexistence, the macrocycle spends longer times over the *fum* station; **b)** F = 9.4 pN ≈ $F_{1/2}$ where both histograms overlap; **c)** F = 9.9 pN > $F_{1/2}$, as expected for forces above coexistence, the macrocycle spends longer times over the *succ* station. **d)** Dependence of shuttling rates with force. As expected from the Bell-Evans model, the shuttling rates from *fum* to *succ* station, k_{fum} (green), and the backward rates, k_{succ} (orange), vary exponentially with force. The intersection point between both linear fits renders the coexistence force, $F_{1/2}$ ≈ 9.4 pN (*N* = 8).

The transit times calculated in the main text and reported in **Figure 2** do not determine the shuttling or kinetic rates between stations. These rates are mainly defined by the lifetime of the macrocycle at each station,[S12,S13] which are 1-2 orders of magnitude longer than the transit-path times, depending on the force applied (compare **Figure S19b** and **d** with **Figure S20a-c**).

The shuttling rates are strongly asymmetric if one state is thermodynamically favorable over the other, as in conditions when force is higher or lower than $F_{1/2}$, (**Figure S20d**). These shuttling rates are related with τ_{tp} following the relation:[S14]

$$\tau_{tp} = \frac{p[tp]}{2k_{fum}P_{fum}} = \frac{p[tp]}{2k_{succ}P_{succ}} \quad \textbf{(equation S3)}$$

where k_{fum} and k_{suc} are the rates for *fum* and *succ* stations (**Table S2**), respectively; P_{fum} and P_{succ} are the equilibrium probabilities to be in the *fum* or *succ* station; and $p[tp]$ is the fraction of time spent on transition paths from the total time of the trace. We retrieved k and P from the extension trajectories at different forces and calculated τ_{tp} following **equation S3** (**Figure S21**). The values obtained are relatively close to the ones measured experimentally from the extension-time trajectories ($b \rightarrow a$: 7.1 ± 3 ms, and $a \rightarrow b$: 6.3 ± 3 ms, **Figure 2** in main text, and **Table S1**). Note that the values obtained in **Figure 2** are dependent on the boundaries a and b defining the transition state, and that were chosen somehow arbitrarily.

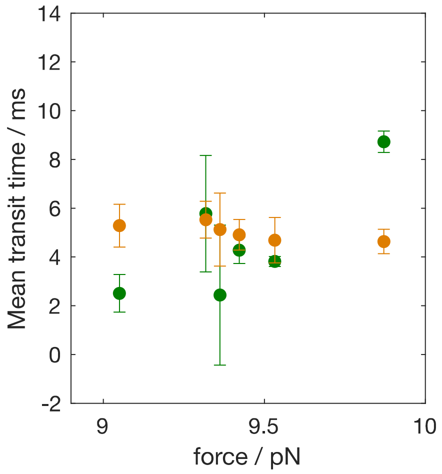

Figure S21: Calculation of τ_{tp} from equation S3. The values of τ_{tp} retrieved in **Figure 2** of main text match to those calculated using **equation S3** assuming kinetic rates and occupation probabilities at each station (orange and green dots, for *succ* and *fum* stations, respectively).

12. Generality of symmetry in transition path distributions

According to the principle of microscopic reversibility, at equilibrium each individual reaction occurs in such a way that the forward and reverse rates are equal. This implies that the number of datapoints (or time) must be equal for opposite trajectories (*a*→*b* and *b*→*a*). The relation $\tau_{LTFT}(a \rightarrow b) = \tau_{LTFT}(b \rightarrow a)$ should hold independently of the boundaries *a* and *b* chosen, as well as the experimental parameters (such as constant force).

Effect of constant force on the LTFT symmetry:

As shown in **Figure 3** in the main text, the distributions of τ_{LTFT} are symmetric at $F_{1/2}$, but also at lower and higher forces, where the equilibrium is shifted towards the *fum* or *succ* stations, respectively. **Table S3** displays the results of the significance tests where, in general, for the 5 forces evaluated, we obtain positive results of the K-S and M-W tests, indicating that no significance differences are found between LTFT time distributions in opposite directions (see **section S7** for details on the test implementation). The case of 9.05 pN fails to pass the K-S test, but it does pass the M-W test and has identical values for median and mean, considering the standard deviations. For 9.49 and 9.88 pN the tests are successful, but they return low prediction powers, due to the small number of events (*n*) forming the histograms.

Force (pN)		9.05	9.33	9.42	9.49	9.88
Boundaries (a⇄b, nm)		-8 ⇄ 8				
$\tau_{LTFT}(a \rightarrow b)$	***n***	113	883	100	44	54
	Mean (ms)	30	25.5	19.8	13.6	28.9
	Median (ms)	26	22	16	12	26
	St. Dev. (ms)	14	14	11	7.6	13
$\tau_{LTFT}(b \rightarrow a)$	***n***	112	884	100	45	55
	Mean (ms)	28	26	17.7	14.6	26.9
	Median (ms)	26	22	16	10	26
	St. Dev. (ms)	18	14	8.2	10	12
K-S Test	***p-val***	0.05	0.59	0.55	0.21	0.68
	power	87%	100%	87%	49%	61%
M-W Test	***p-val***	0.1	0.38	0.4	0.67	0.49
	power	95%	100%	93%	62%	73%

Table S3. Statistical parameters retrieved from the τ_{LTFT} distributions shown in Figure 3 (main text). n corresponds to the number of events (transitions) counted for each trajectory, *St. Dev.* Is the standard deviation. K-S and M-W stand for Kolmogorov-Smirnov and Mann-Whitney tests. Values in red indicate low detection efficiency (or power) or failure passing symmetry tests.

Another example of symmetry holding at different applied forces is presented in **Figure 2** and **section 10**, in this case evaluating narrower boundaries covering the distance between half of the mean positions of *fum* and *succ* stations. Again, the symmetry is generally demonstrated independently from the force, and hence we conclude that it is a general property.

Effect of boundaries on the LTFT symmetry:

The choice of boundaries *a* and *b* should not affect the symmetry of the τ_{LTFT} distributions. Indeed, in **Figure S22**, we include the demonstration of the LTFT principle for generic cases where *a* and *b* are symmetrically chosen (with respect to extension 0 nm) in the *fum* and *succ* stations, respectively, with varying distance between them ranging from 4 to 28 nm. Since the number of successful transitions (**section 9**) depends on the boundaries (the larger the distance between *a* and *b* the less successful transitions within the trace), for this analysis we chose the longest trace available (F = 9.33 pN) in order to increase statistical events and significance of the results. For all cases shown in **Figure S22**, (top panels include a 1s portion of the trace with representative transitions while bottom panels shown the corresponding τ_{LTFT} distributions), τ_{LTFT} show symmetry for forward and backward transitions, confirmed by the statistical significance tests results (**Table S4**).

The symmetry of τ_{LTFT} (and LTFT principle) holds also when the boundaries are chosen asymmetrically (**Figure S23**, and **Table S5** for significance test) to display a transition within the *fum* (**b, f**) or *succ* stations (**a, e**), or a transition from *fum* to *succ* not symmetric to the center (**c, g** and **d, h**). Note that panels e and h in **Figure S23** do not pass the Kolmogorov-Smirnov test (**Table S5**), however, they do pass Mann-Whitney U-test and present identical mean and medians within noise level.

Last, while the results discussed in this section relate to the same trace acquired at 9.33 pN, changing the boundaries *a* and *b* does not affect the symmetry of τ_{LTFT} at any force, as can be inferred for the other examples presented in this work by comparing **Figure 3** in main text with **Figure S19** in section **8**.

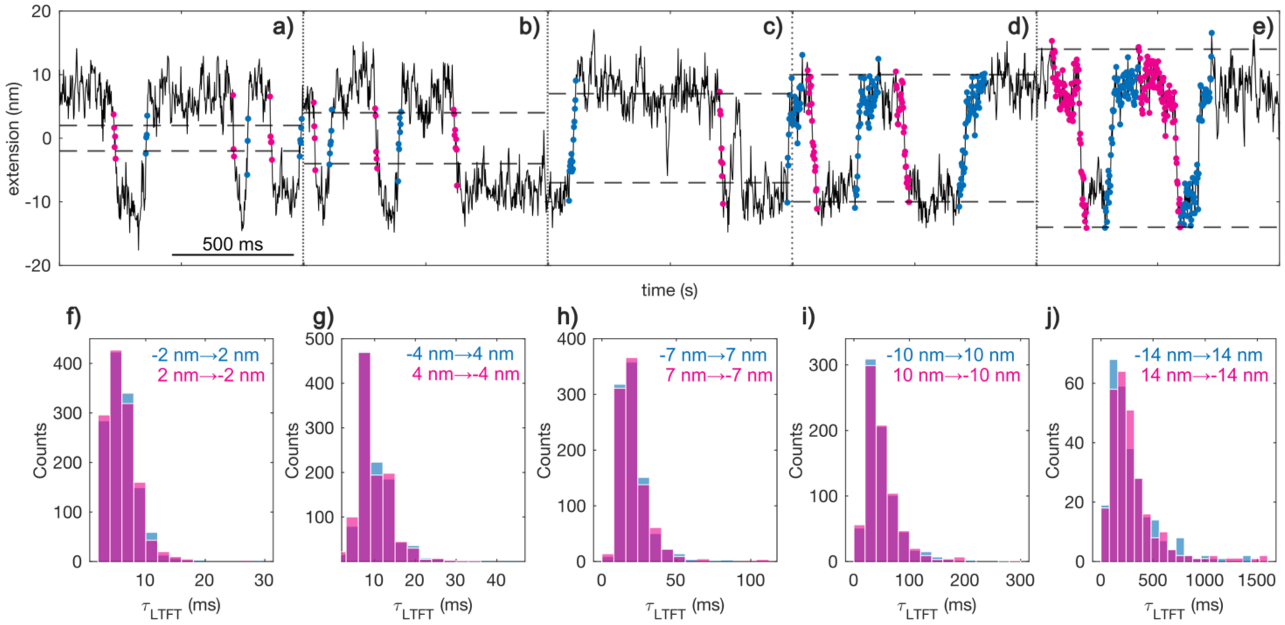

Figure S22: Calculation of LTFT time distributions for varying symmetric boundaries at force 9.33 pN. Top: 1 second trace segment with datapoints corresponding to *a*→*b* and *b*→*a* transitions indicated in blue and pink, respectively (dashed horizontal lines indicate the boundaries, and solid black line corresponds to the data) for *a* and *b:* **a)** ± 2 nm; **b)** ± 2 nm; **c)** ± 7 nm; **d)** ± 10 nm; and **d)** ± 14 nm. **f)-j)** Corresponding distributions of τ_{LTFT} showing symmetry between $a \rightarrow b$ and $b \rightarrow a$ in all cases. Statistical significance tests results are detailed in **Table S4**.

Boundaries ($a \rightleftarrows b$, nm)		-2 ⇄ 2	-4 ⇄ 4	-7 ⇄ 7	-10 ⇄ 10	-14 ⇄ 14
$\tau_{LTFT}(a \rightarrow b)$	***n***	1281	1073	929	757	269
	Mean (ms)	5	9.5	19.6	48.3	287
	Median (ms)	4	8	18	40	220
	St. Dev. (ms)	2.6	4.3	9.4	29.8	224
$\tau_{LTFT}(b \rightarrow a)$	***n***	1281	1074	930	758	270
	Mean (ms)	5	9.2	19.8	48.3	291
	Median (ms)	4	8	18	40	233
	St. Dev. (ms)	2.6	4.1	10.7	30.7	239
K-S Test	***p-val***	0.99	0.51	0.90	0.91	0.47
	power	100%	100%	100%	100%	100%
M-W Test	***p-val***	0.6	0.60	0.97	0.80	0.64
	power	100%	100%	100%	100%	100%

Table S4. Statistical parameters retrieved from the τ_{LTFT} distributions shown in Figure S22. Values correspond to varying symmetric boundaries in the trace acquired at 9.33 pN. n corresponds to the number of events (transitions) counted for each trajectory; *St. Dev.* is the standard deviation. K-S and M-W stand for Kolmogorov-Smirnov and Mann-Whitney tests.

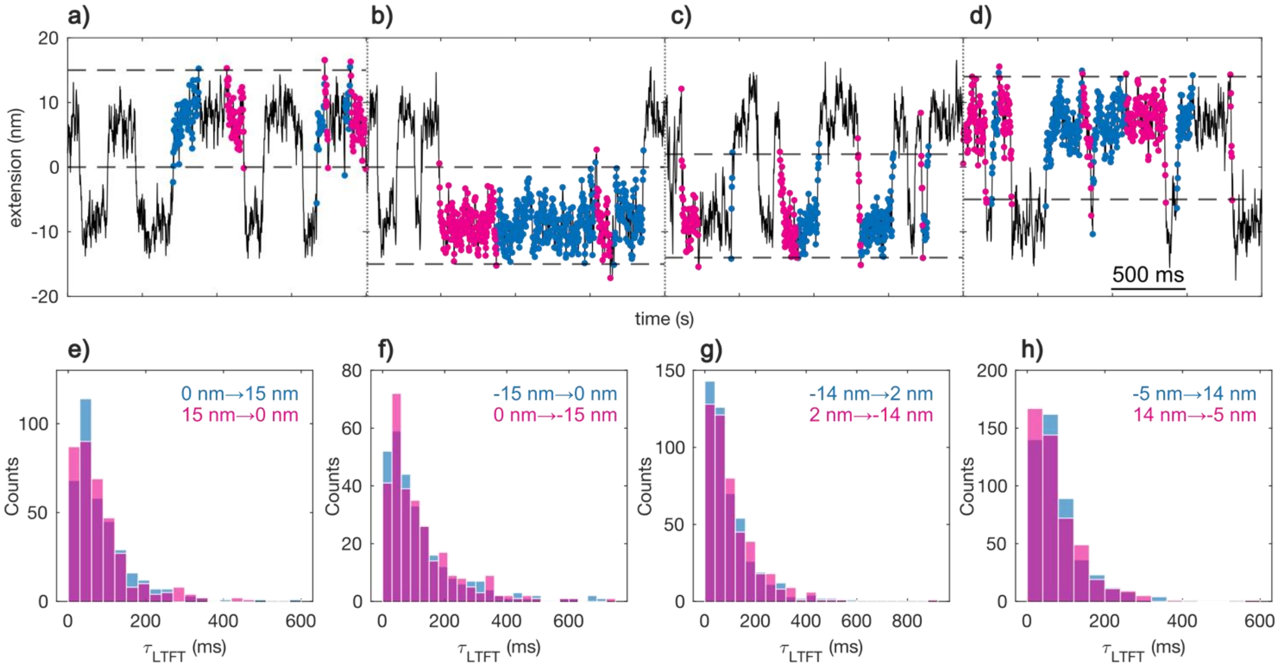

Figure S23: Calculation of LTFT time distributions varying asymmetric boundaries at force 9.33 pN. Top: 2 seconds trace segment with datapoints corresponding to *a*→*b* and *b*→*a* transitions indicated in blue and pink, respectively (dashed horizontal lines indicate the boundaries, and solid black line corresponds to the data) for: **a)** 0 ⇄ 15 nm; **b)** -15 ⇄ 0 nm; **c)** -14 ⇄ 2 nm; **d)** -5 ⇄ 14 nm. **e)-h)** Corresponding distributions of τ_{LTFT} showing symmetry between $a \rightarrow b$ and $b \rightarrow a$ in all cases. Statistical significance tests results are detailed in **Table S5**.

Boundaries (*a*⇄*b*, nm)		0⇄15	-15⇄0	-14⇄2	-5⇄14
$\boldsymbol{\tau_{LTFT}(a \rightarrow b)}$	***n***	364	288	476	477
	Mean (ms)	84	120	98	79.6
	Median (ms)	59	82	70	58
	St. Dev. (ms)	73	121	93	65
$\boldsymbol{\tau_{LTFT}(b \rightarrow a)}$	***n***	364	289	477	478
	Mean (ms)	82	119	105	76.5
	Median (ms)	60	84	74	58
	St. Dev. (ms)	76	112	98	66
K-S Test	***p-val***	0.04	0.75	0.06	0.012
	power	100%	100%	100%	100%
M-W Test	***p-val***	0.23	0.57	0.09	0.11
	power	100%	100%	100%	100%

Table S5. Statistical parameters retrieved from the τ_{LTFT} distributions shown in Figure S23. Values correspond to varying asymmetric boundaries in the trace acquired at 9.33 pN. *n* corresponds to the number of events (transitions) counted for each trajectory, *St. Dev.* Is the standard deviation. K-S and M-W stand for Kolmogorov-Smirnov and Mann-Whitney tests. Values in red indicate failure in passing corresponding symmetry tests.

13. Bier-Astumian relation: energy landscapes.

Following the Bier-Astumian relation (below and eq. 1 in main text) we calculate the energy landscape ΔG (**Figure 4** in main text) of our system by analyzing the trajectories of the macrocycle along the axel at different forces and regimes. In particular, we calculate the probability $P[a \rightarrow b, \Delta t]$ as the probability of the macrocycle reaching a spatial point *b* starting at *a* within a time interval Δt. $P[b \rightarrow a, \Delta t]$ is the probability of reaching the extension *a* within the time interval Δt after crossing *b*.[S15] In order to compute the energy landscape ΔG as a function of extension (**Figure 4** in main text), one needs to compute the mentioned probabilities at different values of *b, i.e.:*

$$\frac{P[a\rightarrow b,\Delta t]}{P[b\rightarrow a,\Delta t]} \approx exp\left(\frac{-\Delta G(b)}{k_B T}\right) \qquad (\textbf{equation S4})$$

We developed a MatLab code that computes both probabilities and the resulting ΔG automatically. This code is openly available at https://hdl.handle.net/20.500.12614/3812.

The inputs for the calculation are:

- a : starting point (extension), several values of *a* can be computed iteratively
- b : end point (extension), several values of *b* can be computed iteratively
- Δx: extension interval

- Δt: time interval

The probabilities $P(a \rightarrow b, \Delta t)$ and $P(b \rightarrow a, \Delta t)$, are calculated for each pair of values a and b in an iterative manner. Starting with a hopping trace (extension, *x*, vs time, *t)*, we find the times at which the trace passes through the extension value $(x = a, t = t_a)$. To do so, we find the datapoints within the space interval $a \pm \Delta x$ i.e. $x \in (a - \Delta x, a + \Delta x)$ (since experimental traces are limited by an acquisition rate of 0.5 kHz, the trace can pass through *a* without having a datapoint exactly at that value). In our analysis, Δx has been chosen 0.3 nm. Next, we examine the datapoints within the time interval Δt following each t_a value found in the previous step, ie. $t \in (t_a, t_a + \Delta t)$, and investigate the extension values to find out if the trace reaches the value *b* within Δt after having crossed the point *a*. The probability $P(a \rightarrow b, \Delta t)$ is computed as the number of times that the transition *a* → *b* occurs, divided by the number of times that the trace crosses the point *a*. In a similar way, we compute $P(b \rightarrow a, \Delta t)$ as the number of times that the transition *b* → *a* occurs, divided by the number of times that the trace crosses the point *b*. The code is built such that several values of *a* and *b* can be set as input, and the probabilities are computed for each pair of values individually. For a given value of a, we calculate the pair of probabilities $P(a \rightarrow b, \Delta t)$ and $P(b \rightarrow a, \Delta t)$ for all the different values of *b* defined by the user (we set *b* values from -15 to 15 nm in intervals of 0.5 nm), and compute ΔG as the logarithm of the probability ratio (**Figure S24a-c**). Then, we repeat the process for different values of *a* (**Figure S24d-f**). The ΔG reported in Figure 4 of the main text is the result of averaging all the ΔGs calculated for each value of *a*.

Figure S24 shows the dependence of probabilities and ΔG on *b* for different values of Δt and *a*. Particularly, $P(a \rightarrow b, \Delta t)$, $P(b \rightarrow a, \Delta t)$ and the corresponding $\frac{\Delta G}{K_B T} = -\ln(P(a \rightarrow b, \Delta t)/P(b \rightarrow a, \Delta t))$ for *a*=5 nm and decreasing time interval are presented in **Figure S24a-c** as a function of the value of *b*, respectively. Alternatively, the same is plotted in **Figure S24d-f** for a fixed time interval of 0.05 s and different starting points *a*.

As expected, decreasing the time interval will increase the noise of the calculated probabilities and the energy landscape due to a reduced number of events, or counts, for the considered transitions in a narrower time frame. The selected starting point (**Figure S24d-f**) determines which range of extension is better resolved (i.e. when *a* = -5 nm/pink, larger probabilities are found for transitions close to *b*=-5 nm, which will result in a better resolved energy landscape around that value). As the final extension value (*b*) gets further from the initial point, the probability of finding a successful transition *a* → *b* decreases. Therefore, by running the calculation over a large range of *a* and averaging the energy profiles obtained for each *a,* we obtain an averaged ΔG included in **Figure 4** in the main text.

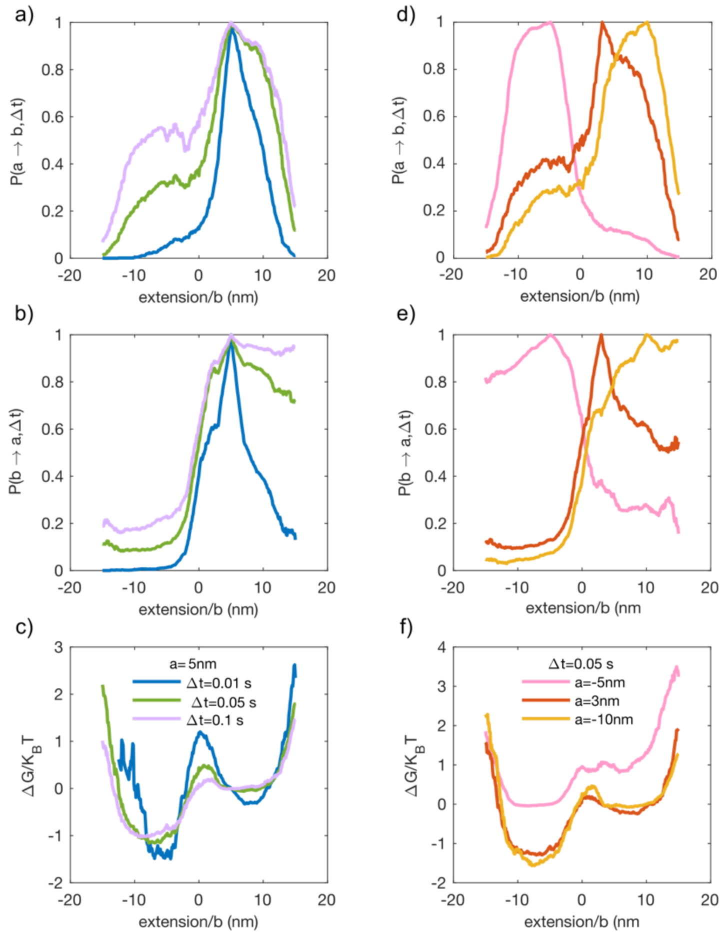

Figure S24: Calculation of energy landscapes using the Bier-Astumian relation: a) $P[a \rightarrow b, \Delta t]$, **b)** $P[b \rightarrow a, \Delta t]$ and **c)** the corresponding ΔG for *a*=5 nm and decreasing time interval (0.01 s blue, 0.05 s green and 0.1 s purple). **d)** $P[a \rightarrow b, \Delta t]$, **e)** $P[b \rightarrow a, \Delta t]$ and **f)** the corresponding ΔG for *a*=-5 nm (pink), 3 nm (red) and 10 nm (yellow) at a fixed time interval of 0.05 s.

14. Implications of Bier-Astumian formalism for the investigation of molecular shuttles out of equilibrium.

The equation described as the Bier-Astumian relation arises from the principle of microscopic reversibility. There are two major results derived by Bier and Astumian from the Onsager-Machlup treatment of over-damped (low Reynolds number) stochastic processes for single particles. The first result is the equality between the last touch first touch times from *a* to *b*, and from *b* to *a*, irrespective of their relative energies ($\mathrm{G_a}$ and $\mathrm{G_b}$)

$$\tau_{\mathrm{LTFT}}(\mathrm{a} \rightarrow \mathrm{b}) = \tau_{\mathrm{LTFT}}(\mathrm{b} \rightarrow \mathrm{a}) \qquad \textbf{(equation S5)}$$

The validity of this equality does not rely on the positional distribution of the system having relaxed to equilibrium, i.e., on the system being in thermodynamic equilibrium characterized by a Boltzmann equation. The requirement is that the dynamics are over-damped – i.e., that the velocity distribution function relaxes to equilibrium, i.e., to a Maxwell-Boltzmann velocity distribution, on a very fast time-scale.

The second result is the ratio between the conditional probabilities to go from one state to another,

$$\frac{\mathrm{P(a{\rightarrow}b,\Delta t)}}{\mathrm{P(b{\rightarrow}a,\Delta t)}} = \mathrm{e}^{-\Delta \mathrm{G_{ab}/RT}} \qquad \textbf{(equation S6)}$$

An important point to note is that while both the numerator and the denominator on the left-hand side of the equation depend strongly on Δt, their ratio, expressed on the right-hand side of the equation, does not, and is hence valid for any Δt. This equality is valid without any assumption of the system being in thermodynamic equilibrium, only mechanical equilibrium – i.e. that it undergoes low Reynolds number motion (viscosity dominates over inertia). By choosing different values for *a* and *b* we were able to use the trajectory data obtained to make a plot of free energy *vs* position as shown in **Figure 4** of the main text. We compared this plot with a plot calculated using the Boltzmann equation:

$$\frac{\mathrm{P_{eq}(a)}}{\mathrm{P_{eq}(b)}} = \mathrm{e}^{-\Delta \mathrm{G_{ab}/RT}} \qquad \textbf{(equation S7)}$$

which is based on the system being in thermodynamic equilibrium, i.e., on the positional distribution having relaxed to its equilibrium value. **Equation S6** holds irrespective of whether the positional distribution has relaxed to equilibrium – there is no requirement that the system be in thermodynamic equilibrium. In contrast, **equation S7** is valid only in the long-time limit, i.e., at thermodynamic equilibrium. Nevertheless, these two different approaches for determining the free-energy landscape give rise to computationally identical results when used to map the free-energy landscape under our experimental conditions as shown in **Figure 4** of our manuscript.

Leigh and colleagues examined an experimental system in which chemical energy from conversion of a carbodiimide (DIC) to a urea (UIC).[S16-S19] When the “fueling” reaction $\mathrm{DIC} \rightarrow \mathrm{UIC}$ is away from equilibrium the continual dissipation can maintain the distribution between the ring occupancy away from the thermodynamic equilibrium Boltzmann distribution. Their system is shown below (**Figure S25**).

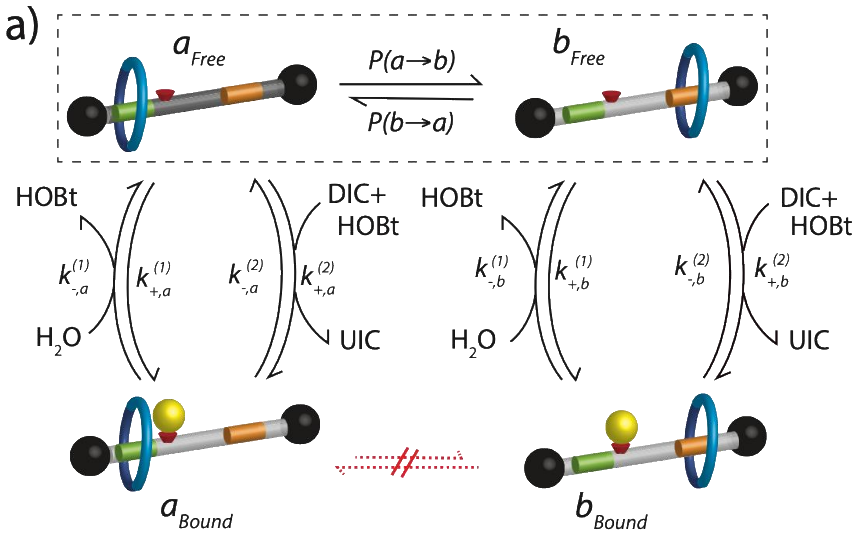

Figure S25: Example from D. A. Leigh and colleagues.[S16-S19]

The key idea is that there is a catalytic installation of a protecting group HOBt concomitant with the exergonic conversion of DIC to UIC. The presence of the protecting group, HOBt, influences the kinetics – the relative barrier heights for transitions – but not the thermodynamics – the relative energies of the states *a* and *b*, G_a and G_b. The distribution between the occupancy on *a* and *b* is shifted away from equilibrium by the continual dissipation due to the conversion $\mathrm{DIC} \to \mathrm{UIC}$, and does not obey the Boltzmann distribution, **equation S7**, but instead obeys the non-equilibrium pumping equality:

$$\frac{P_{ss}(a_{Bound})}{P_{ss}(b_{Bound})} = e^{-\Delta G_{ab}/RT}\langle e^{\mathcal{W}_{pd,\mathcal{S}_{ab}}/RT}\rangle \qquad \text{(equation S8)}$$

which for the specific kinetic diagram shown can be written as:

$$\frac{P_{ss}(a_{Bound})}{P_{ss}(b_{Bound})} = \overbrace{\left[\frac{P(a_{free} \to b_{free})}{P(b_{free} \to a_{free})}\right]}^{e^{-\Delta G_{ab}/RT}} \left[\frac{(q\,e^{\Delta\mu/RT}+1)+N}{(q+e^{\Delta\mu/RT})+N}\right] \qquad \text{(equation S9)}$$

where $\Delta\mu = \mu_{DIC} + \mu_{H_2O} - \mu_{UIC}$ parametrizes the energy input from the exergonic reaction, $q = \frac{k^{(1)}_{-,a}k^{(2)}_{-,b}}{k^{(2)}_{-,a}k^{(1)}_{-,b}}$ parametrizes the kinetic bias that dictates whether *a* or *b* is favored relative to equilibrium by the dissipation, and N parametrizes the uncoupling.

At Steady-state the condition:

$$P_{ss}(a_{Bound})P(a_{Bound} \to b_{Bound}, \Delta t) = P_{ss}(b_{Bound})P(b_{Bound} \to a_{Bound}, \Delta t) \qquad \text{(equation S10)}$$

holds for all Δt. The local or generalized detailed balance hypothesis claims that the ratio of forward to backward transition probabilities, which is equal to the ratio of forward to backward net rate constants, is given by the simple relation like the Bier-Astumian relation (**equation S6**), but modified by the exponential of the “non-dimensional change in entropy of the mediating reservoir”, or the “dissipated free energy” σ_{ab},

$$\frac{P(a_{Bound} \to b_{Bound}, \Delta t)}{P(b_{Bound} \to a_{Bound}, \Delta t)} = e^{-\Delta G_{ab}/RT} e^{\sigma_{ab}} \qquad \textbf{(equation S11)}$$

This claim **is not in general true**, but does hold in the special limit that q, the kinetic bias in Eq. 5, approaches infinity, where we identify $\sigma_{ab} = \Delta\mu/RT$. The correct expression is:

$$\frac{P(a_{Bound} \to b_{Bound}, \Delta t)}{P(b_{Bound} \to a_{Bound}, \Delta t)} = e^{-\Delta G_{ab}/RT} \left[\frac{(q\, e^{\Delta\mu/RT} + 1) + N}{(q + e^{\Delta\mu/RT}) + N}\right] \qquad \textbf{(equation S12)}$$

This expression would allow obtaining ΔG and the free-energy landscape of the shuttling reaction upon measuring the forward and backwards transitions probabilities of the macrocycle under conditions away from thermodynamic equilibrium.

.

15. References.

S1. Naranjo, T., Lemishko, K.M., de Lorenzo, S., Somoza, A., Ritort, F., Perez, E.M., and Ibarra, B. (2018). Dynamics of individual molecular shuttles under mechanical force. Nat. Commun. *9*, 4512. 10.1038/s41467-018-06905-8.

S2. M. J. Frisch, G.W.T., H. B. Schlegel, G. E. Scuseria, M. A. Robb, J. R. Cheeseman, G. Scalmani, V. Barone, G. A. Petersson, H. Nakatsuji, X. Li, M. Caricato, A. Marenich, J. Bloino, B. G. Janesko, R. Gomperts, B. Mennucci, H. P. Hratchian, J. V. Ortiz, A. F. Izmaylov, J. L. Sonnenberg, D. Williams-Young, F. Ding, F. Lipparini, F. Egidi, J. Goings, B. Peng, A. Petrone, T. Henderson, D. Ranasinghe, V. G. Zakrzewski, J. Gao, N. Rega, G. Zheng, W. Liang, M. Hada, M. Ehara, K. Toyota, R. Fukuda, J. Hasegawa, M. Ishida, T. Nakajima, Y. Honda, O. Kitao, H. Nakai, T. Vreven, K. Throssell, J. A. Montgomery, Jr., J. E. Peralta, F. Ogliaro, M. Bearpark, J. J. Heyd, E. Brothers, K. N. Kudin, V. N. Staroverov, T. Keith, R. Kobayashi, J. Normand, K. Raghavachari, A. Rendell, J. C. Burant, S. S. Iyengar, J. Tomasi, M. Cossi, J. M. Millam, M. Klene, C. Adamo, R. Cammi, J. W. Ochterski, R. L. Martin, K. Morokuma, O. Farkas, J. B. Foresman, and D. J. Fox. Gaussian 09, Gaussian, Inc., Wallingford CT, 2016.

S3. Morin, J.A., Cao, F.J., Lázaro, J.M., Arias-Gonzalez, J.R., Valpuesta, J.M., Carrascosa, J.L., Salas, M., and Ibarra, B. (2012). Active DNA unwinding dynamics during processive DNA replication. Proc. Natl. Acad. Sci. U.S.A. *109*, 8115-8120.
10.1073/pnas.1204759109.

S4. Smith, S.B., Cui, Y., and Bustamante, C. (2003). [7] Optical-trap force transducer that operates by direct measurement of light momentum. In Methods Enzymol., (Academic Press), pp. 134-162.

S5. Gore, J., Bryant, Z., Nöllmann, M., Le, M.U., Cozzarelli, N.R., and Bustamante, C. (2006). DNA overwinds when stretched. Nature, *442*, 836-839.
10.1038/nature04974.

S6. Smith, S.B., Finzi, L., and Bustamante, C. (1992). Direct mechanical measurements of the elasticity of single DNA molecules by using magnetic beads. Science, *258*, 1122-1126.
10.1126/science.1439819.

S7. Gladrow, J., Ribezzi-Crivellari, M., Ritort, F., and Keyser, U.F. (2019). Experimental evidence of symmetry breaking of transition-path times. Nat. Commun. *10*, 55.
10.1038/s41467-018-07873-9.

S8. Jean Dickinson Gibbons, S.C. (2010). Nonparametric Statistical Inference (5th Ed., Boca Raton, FL: Chapman & Hall/CRC Press, Taylor & Francis Group.).

S9. Massey Jr, F.J. (1951). The Kolmogorov-Smirnov Test for Goodness of Fit. J. Am. Stat. Assoc. *46*, 68-78. 10.1080/01621459.1951.10500769.

S10. Merkel, R., Nassoy, P., Leung, A., Ritchie, K., and Evans, E. (1999). Energy landscapes of receptor-ligand bonds explored with dynamic force spectroscopy. Nature, *397*, 50-53. 10.1038/16219.

S11. Evans, E. (2001). Probing the Relation Between Force—Lifetime—and Chemistry in Single Molecular Bonds. Annu. Rev. Biophys. Biomol. Struct. *30*, 105-128. 10.1146/annurev.biophys.30.1.105.

S12. Kramers, H.A. (1940). Brownian motion in a field of force and the diffusion model of chemical reactions. Physica, *7*, 284-304. 10.1016/S0031-8914(40)90098-2

S13. Hänggi, P., Talkner, P., and Borkovec, M. (1990). Reaction-rate theory: fifty years after Kramers. Rev. Mod. Phys. *62*, 251-341. 10.1103/RevModPhys.62.251.

S14. Neupane, K., Foster, D.A.N., Dee, D.R., Yu, H., Wang, F., and Woodside, M.T. (2016). Direct observation of transition paths during the folding of proteins and nucleic acids. Science, *352*, 239-242. 10.1126/science.aad0637.

S15. Confesor, M.N.P. (2015). Bier-Astumian relation, fluctuation theorem and their possible applications. Int. J. Mod. Phys.: Conf. *36*, 1560009. 10.1142/S2010194515600095.

S16. Binks, L., Borsley, S., Gingrich, T.R., Leigh, D.A., Penocchio, E., and Roberts, B.M.W. (2023). The role of kinetic asymmetry and power strokes in an information ratchet. Chem, *9*, 2902-2917. 10.1016/j.chempr.2023.05.035

S17. Astumian, R.D. (2023). Nonequilibrium steady states, ratchets, and kinetic asymmetry. Matter *6*, 2533-2536. 10.1016/j.matt.2023.07.007

S18. Astumian, R.D. (2024). Kinetic Asymmetry and Directionality of Nonequilibrium Molecular Systems. Angew. Chem. Int. Ed. *63*, e202306569. 10.1002/anie.202306569

S19. Astumian, R.D. (2010). Thermodynamics and Kinetics of Molecular Motors. Biophys. J. *98*, 2401-2409. 10.1016/j.bpj.2010.02.040.